DE-FG05-80ET-53088-657 IFSR #657

Momentum-Energy Transport from Turbulence Driven by Parallel Flow Shear

J.Q. DONG and W. HORTON
Institute for Fusion Studies
The University of Texas at Austin
Austin, Texas 78712
and
R.D. BENGTSON and G.X. LI
Fusion Research Center
The University of Texas at Austin
Austin, Texas 78712

April 1994

Momentum–energy transport from turbulence driven by parallel flow shear

J.Q. Dong,[a] W. Horton
Institute for Fusion Studies
The University of Texas at Austin
Austin, Texas 78712
and
Roger D. Bengtson and G.X. Li
Fusion Research Center
The University of Texas at Austin
Austin, Texas 78712

Abstract

The low frequency $\mathbf{E} \times \mathbf{B}$ turbulence driven by the shear in the mass flow velocity parallel to the magnetic field is studied using the fluid theory in a slab configuration with magnetic shear. Ion temperature gradient effects are taken into account. The eigenfunctions of the linear instability are asymmetric about the mode rational surfaces. Quasilinear Reynolds stress induced by such asymmetric fluctuations produces momentum and energy transport across the magnetic field. Analytic formulas for the parallel and perpendicular Reynolds stress, viscosity and energy transport coefficients are given. Experimental observations of the parallel and poloidal plasma flows on TEXT-U are presented and compared with the theoretical models.

Pacs nos.: 52.25.Fi, 52.35.Qz, 52.35.Ra, 52.55.Fa

[a]Permanent address: Southwestern Institute of Physics, Chengdu, China

I. Introduction

Since it was first studied in early 1970's,[1] the instability driven by the cross-field gradient (shear) of the plasma mass flow velocity parallel to the magnetic field in an inhomogeneous plasma has been investigated extensively in fusion[2–6] as well as in space plasmas.[7,8] Such instability can be strongly driven by neutral-beam-injection in tokamak discharges. In addition, a strong gradient of the flow velocity may appear near the plasma boundary due to the presence of the limiter or divertor which is known to dramatically alter the plasma dynamics in the scrape off layer (the shadow of the poloidal limiter or the divertor region) from that in the bulk . In space plasmas, high streaming velocities parallel to the magnetic field and rapid variation of the parallel flow velocity with the distance perpendicular to the magnetic field are measured in the plasma sheet boundary layer due to the influence of the solar wind on the plasma sheet.[8,9]

Such turbulence driving mechanisms are understood and the characteristics of the instability are well documented.[1–9] In this work the emphasis is not on the study of the instability itself but rather on momentum and energy fluxes described by the turbulence induced Reynolds stress. From the Reynolds stress parallel and perpendicular to the magnetic field we determine the associated viscosity and energy transport coefficients generated by the turbulence of the instability. The transport coefficients are characterized both by their magnitude at the mixing length level of the turbulence and by their dimensionless ratios, the Prandtl numbers, which are independent of the turbulence level.

It was first observed on the TEXT tokamak[10] that a poloidal flow shear is formed at the plasma edge. Such flow shear may suppress the plasma density fluctuations and affect the local plasma confinement improvement. Later, the L-mode to H-mode (L-H) transition in tokamak plasma confinement was found to be related to the presence of the poloidal flow

shear near the plasma edge.[11] Theoretical work has been carried out to study the poloidal flow shear effect on the plasma turbulence.[12]

Several possible sources for the generation of such poloidal flow shear have been proposed.[13–20] Among them two models are widely studied. One is the particle losses caused by the interaction with the limiter or divertor.[13,14] An alternative explanation is the Reynolds stress produced by the turbulence in the plasma.[15,16] This latter mechanism requires a physical driving force for the turbulence. A few physical models such as drift-resistive ballooning mode,[19] resistive pressure-gradient driven mode[20] have been proposed and studied.

In this work, the parallel velocity shear, combined with the ion temperature gradient, is proposed as the driving mechanism for the poloidal sheared flow. It has been pointed out by several authors[15,20] that there must be a symmetry breaking mechanism such as boundary conditions in drift waves, or some symmetry breaking seed introduced in the study of pressure-gradient driven turbulence in order to generate nonzero Reynolds stress from fluctuations. One of the features for the model proposed in this work is that the mode eigenfunction is intrinsically asymmetric about the mode rational surface so that the Reynolds stress generation is independent of, or at least not sensitive to, boundary conditions. Symmetry breaking seeds are not needed even in the nonlinear simulations.[6]

Experimental measurements of the parallel and poloidal flows are carried out on Texas Experimental Tokamak Upgrade (TEXT-U) and some of the results are presented in this work. The measurements from a Mach probe show that there is a strong radial gradient of the parallel ion mass flow at about the same region as the poloidal shear layer. The sharp spatial gradient may be created and maintained by the transition from a confined interior plasma to a scrape-off layer plasma regulated by the cold plasma sheath surrounding the limiter. The sheath condition on the net parallel plasma electric current requires the build up of a parallel ion velocity to a fraction of the ion acoustic speed. The turbulence is now driven by the free energy associated with the radial gradient of the parallel flow velocity,

and in turn, produces an acceleration in the poloidal direction. The preliminary evidence that the plasma parallel velocity changes at about the same radial position as the poloidal shear layer supports this scenario for the poloidal shear flow generation. The theoretical results are compared with and shown to be in reasonable agreement with the experimental observations if a neoclassical damping mechanism is introduced to balance the driving force from the Reynolds stress.

In large tokamaks the toroidal velocity gradients are measured by spectroscopic techniques and may be driven in the interior by parallel beam injection. In a recent analysis of the high poloidal beta discharge regime on JT-60U,[21] a transport barrier is reported at the $q = 3$ surface where the toroidal velocity gradient, measured in terms of the dimensionless stability parameter defined here, has a value close to that found in the TEXT-U scrape-off layer. We speculate that same physical processes proposed here for local confinement improvement on TEXT-U may be involved in the transport barrier generation on JT-60U.

The remainder of this work is organized as follows. In Sec. II the physics model is described, and the eigenmode equation is given and solved analytically. Analytic formulas for the Reynolds stress are derived in Sec. III and the numerical evaluations are presented in Sec. IV. In Sec. V the experimental observations on TEXT-U are presented and possible correlation of the theoretical results obtained in this work with these experiments are discussed in detail while Sec. VI is devoted to the conclusions of this study.

II. Physics Model and Eigenmode Equation

We consider a slab magnetic configuration $\mathbf{B} = B_0(\hat{\mathbf{z}} + \frac{x}{L_s}\hat{\mathbf{y}})$, where L_s is the scale length of magnetic shear. Here the x-, y-, and z-directions in the sheared slab geometry are defined as the radial, poloidal and toroidal directions in the tokamak configuration. Fluid theory is used to describe the ion motion and the electrons are adiabatic. Equilibrium parallel velocity shear $dv_\parallel(x)/dx = \text{const.}$ is considered and ion temperature gradient (η_i) effects

are included in the instability study. The perturbed electrostatic potential is expressed as $\tilde{\phi}(x,y,t) = \mathrm{Re}\{\phi(x)\exp(ik_y y - i\omega t)\}$. Under these assumptions it is straightforward to derive the linear eigenmode equation for the function $\phi(x)$ as follows,[4]

$$\frac{d^2\phi(x)}{dx^2} - b_s\phi(x) + \frac{1-\widehat{\omega}}{\widehat{\omega}+K}\phi(x) + \left[\frac{s^2x^2}{\widehat{\omega}^2} - \frac{\widehat{v}'_{0\|}sx}{(\widehat{\omega}+K)\widehat{\omega}}\right]\phi(x) = 0\ , \tag{1}$$

where $b_s = k_y^2\rho_s^2$, $\widehat{\omega} = \omega/\omega_{*e}$, $K = (1+\eta_i)/\tau$, $\tau = T_e/T_i$, $\eta_i = d\ \ln\ T_i/d\ \ln\ n$, $\omega_{*e} = k_y\rho_s c_s/L_n$ is the electron diamagnetic frequency, x is normalized to $\rho_s = c_s/\Omega = (T_e/m_i)^{\frac{1}{2}}/\Omega = c(m_iT_e)^{\frac{1}{2}}/eB$, Ω is the ion gyrofrequency; $\widehat{v}'_{0\|} = L_n dv_{\|}/c_s dx$, $s = L_n/L_s$ with L_n being the density gradient scale length. Here T_e and T_i are the electron and ion temperature, respectively. Equation (1) is valid in the hydrodynamic-like limit and the full kinetic equation is also given in Ref. 4.

The dispersion relation obtained from Eq. (1) is

$$\left[-b_s + \frac{1-\widehat{\omega}}{\widehat{\omega}+K} - \frac{\widehat{v}'^2_{0\|}}{4(\widehat{\omega}+K)^2}\right]\frac{\widehat{\omega}}{is} = 2n+1\ . \tag{2}$$

The corresponding eigenfunction is

$$\phi^{(n)}(x) = \phi_0^{(n)}\frac{\widehat{\omega}}{is}H_n\left((is/\widehat{\omega})^{\frac{1}{2}}(x+\Delta)\right)e^{-is(x+\Delta)^2/2\widehat{\omega}}\ , \tag{3}$$

where H_n is the Hermite function of order n and

$$\Delta = -\frac{\widehat{v}'_{0\|}\widehat{\omega}}{2s(\widehat{\omega}+K)}\ . \tag{4}$$

In the rest of this work only the $n=0$ mode will be considered.

It is easy to notice that the mode growth rate is independent of the sign of $\widehat{v}'_{0\|}$ from Eq. (2). However, the asymmetry element, the shift Δ of the position of the maximum $\phi^{(0)}(x)$ from the mode rational surface ($x=0$), depends on the sign of $\widehat{v}'_{0\|}$ and is important for the Reynolds stress calculation. For cold ion approximation ($K\to 0$) Δ is a real shift in x-space. In general Δ is complex and introduces a deformation of the eigenfunction given by $\mathrm{Re}\left\{\phi^{(n)}(x)\exp(ik_y y - i\omega t)\right\}$ as well as the shift.

III. Equations for Reynolds Stress

The general expression for the perturbed electrostatic potential is $\tilde{\phi} = \mathrm{Re}\{\sum_{k_y} \phi_0 \phi(x) \exp(-i\omega t + ik_y y)\}$. The $\mathbf{E} \times \mathbf{B}$ drift velocity is

$$\tilde{v}_x = -\frac{c}{B}\frac{\partial \tilde{\phi}}{\partial y}, \qquad \tilde{v}_y = \frac{c}{B}\frac{\partial \tilde{\phi}}{\partial x}, \tag{5}$$

where B is the toroidal magnetic field and c is the speed of light. In the representation of $\tilde{\phi}$ we use ϕ_0 to characterize the rms fluctuation level and $\phi(x)$ the normalized wave function.

Now we introduce the two components of the micro-Reynolds stress that measure the radial flux of the parallel and perpendicular momentum,

$$\pi_{xy}(x) = \tilde{v}_x^* \tilde{v}_y + \tilde{v}_x \tilde{v}_y^*, \tag{6}$$

$$\pi_{x\|}(x) = \tilde{v}_x^* \tilde{v}_\| + \tilde{v}_x \tilde{v}_\|^*, \tag{7}$$

where in the quasilinear approximation $\tilde{v}_\| = (esc_s/T_e\hat{\omega})x\tilde{\phi}$. In writing Eqs. (6) and (7) we leave implicit the summation over all poloidal mode numbers and all rational surfaces determined by the toroidal mode number spectrums. It is straightforward to obtain the analytic expressions for Eqs. (6) and (7), using Eqs. (3) and (5), as follows:

$$\pi_{xy} = |\phi_0|^2 \frac{c^2}{\rho_s B^2}\frac{2k_y}{s}(2x\hat{\omega}_r + \Delta\hat{\omega}^* + \Delta^*\hat{\omega}) e^{is[\hat{\omega}(x+\Delta^*)^2 - \hat{\omega}^*(x+\Delta)^2]/2|\hat{\omega}|^2}, \tag{8}$$

$$\pi_{x\|} = |\phi_0|^2 \frac{cc_s e}{BT_e}\frac{x}{s}(-2k_y\gamma) e^{is[\hat{\omega}(x+\Delta^*)^2 - \hat{\omega}^*(x+\Delta)^2]/2|\hat{\omega}|^2}, \tag{9}$$

where $*$ stands for complex conjugate, $\hat{\omega}_r$ and γ are the real and imaginary part of $\hat{\omega}$, respectively.

For energy transport we need the radial flux $q_x(x)$ of the ion pressure fluctuation

$$q_x(x) = \tilde{v}_x^* \tilde{p} + \tilde{v}_x \tilde{p}^* = |\phi_0|^2 \frac{P_0(1+\eta_i)c^2}{\rho_s c_s B^2}\frac{2\gamma k_y}{s^2} e^{is[\hat{\omega}(x+\Delta^*)^2 - \hat{\omega}^*(x+\Delta)^2]/2|\hat{\omega}|^2}, \tag{10}$$

where again we use the quasilinear approximation $\widetilde{p} = -\widetilde{v}_x dP_0/i\omega dx$ for the perturbation of the pressure. Here P_0 is the equilibrium pressure and the equilibrium pressure gradient is $dP_0/dx = -KP_0/L_n$.

All the quantities given in Eqs. (8)–(10) are function of $x = r - r_0$ with r_0 being the position of the mode rational surface. In order to obtain the effects of these quantities on the macro-motion, or background motion, these micro-fluxes that are localized to small layers around the resonant surfaces ($x + \Delta = 0$) must be integrated over x. The results are the corresponding values used in the macro-motion equation on the mode rational surface.

In this way we have

$$\langle \pi_{xy} \rangle = \int_{-\infty}^{+\infty} \left(\widetilde{v}_x^* \widetilde{v}_y + \widetilde{v}_x \widetilde{v}_y^* \right) dx = -|\phi_0|^2 \frac{c^2 k_y}{B^2 \rho_s} \frac{\sqrt{\pi} |\widehat{\omega}|^3 K \widehat{v}'_{0\parallel}}{s^{\frac{5}{2}} \gamma^{\frac{1}{2}} |\widehat{\omega} + K|^2} e^{\gamma \widehat{v}_{0\parallel}^2 K^2 / 4s |\widehat{\omega} + K|^4} , \qquad (11)$$

$$\langle \pi_{x\parallel} \rangle = \int_{-\infty}^{+\infty} \left(\widetilde{v}_x^* \widetilde{v}_\parallel + \widetilde{v}_x \widetilde{v}_\parallel^* \right) dx = -|\phi_0|^2 \frac{c c_s e}{B T_e s^{\frac{5}{2}}} \sqrt{\pi} \frac{k_y \gamma^{\frac{1}{2}} |\widehat{\omega}|^3 \widehat{v}'_{0\parallel}}{|\widehat{\omega} + K|^2} e^{\gamma \widehat{v}_{0\parallel}^2 K^2 / 4s |\widehat{\omega} + K|^4} , \qquad (12)$$

and

$$\langle q_x \rangle = \int_{-\infty}^{+\infty} \left(\widetilde{v}_x^* \widetilde{p} + \widetilde{v}_x \widetilde{p}^* \right) dx = |\phi_0|^2 \frac{P_0 (1 + \eta_i) c^2}{\rho_s c_s B^2} \frac{(\pi\gamma)^{\frac{1}{2}} |\widehat{\omega}| k_y}{s^{\frac{5}{2}}} e^{\gamma \widehat{v}_{0\parallel}^2 K^2 / 4s |\widehat{\omega} + K|^4} . \qquad (13)$$

In Eqs. (11)–(13) the mode growth rate γ and real frequency $\widehat{\omega}_r$ must be obtained from the mode dispersion equation (2) (with $\widehat{\omega} = \widehat{\omega}_r + i\gamma$), for each k_y and the mean fluxes summed over all k_y.

Apparently, $\langle \pi_{xy} \rangle$ and $\langle \pi_{x\parallel} \rangle$ vanish linearly with $\widehat{v}'_{0\parallel} \to 0$ while $\langle q_x \rangle$ does not. Considering that the ion temperature gradient is taken into account, the instability is still possible under such limit. This clearly shows the importance of the parallel velocity shear for the momentum transport from turbulence in the quasilinear theory.

With this presentation of $\langle \pi_{xy} \rangle$, $\langle \pi_{x\parallel} \rangle$, and $\langle q_x \rangle$ we are giving the intensity for per unit spectrum of the fluctuations at the specified k_y. The complete flux is then the integral of the intensity over the spectral distribution of the fluctuations $\int I(k_y) dk_y$. When one scale

dominates the fluctuation spectrum it is adequate to take ϕ_0^2 as the rms amplitude and choose k_y corresponding to the dominant scale.

In integrating the micro fluxes over x we obtain the weight for a single rational surface. To obtain the total flux across the sheared magnetic field, we must introduce the mean density of the rational surfaces[22] $\rho_{k_y}(r) = (6|q'|/\pi^2 q^2)k_y r$ and define $\langle \pi_{xy} \rangle = \sum_{k_y} \int \rho_{k_y}(r)\pi_{xy} dr$. Note that $\rho_{k_y}(r)$ varies only on the scale of $q(r)$ and is then essentially constant over the shear flow layer and the mode width. The total fluxes is given by the integrated formulas Eqs. (11)–(13) multiplied by the function $\rho_{k_y}(r)$ and summed over all k_y. Here we report the flux per unit of these weighting factors.

The momentum transport coefficients $\mu_\perp$ and $\mu_\parallel$ are defined by

$$\mu_\perp = \frac{\langle \pi_{xy} \rangle}{-\frac{dv_\parallel}{dx}} = |\phi_0|^2 \frac{c^2 k_y (\pi)^{\frac{1}{2}} |\widehat{\omega}|^3 K L_n}{c_s B^2 \rho_s s^{\frac{5}{2}} \gamma^{\frac{1}{2}} |\widehat{\omega} + K|^2} e^{\gamma \widehat{v}_{0\parallel}^2 K^2 / 4s|\widehat{\omega}+K|^4} , \tag{14}$$

and

$$\mu_\parallel = \frac{\langle \pi_{x\parallel} \rangle}{-\frac{dv_\parallel}{dx}} = |\phi_0|^2 \frac{cek_y(\pi)^{\frac{1}{2}} |\widehat{\omega}|^3 L_n \gamma^{\frac{1}{2}}}{BT_e s^{\frac{5}{2}} |\widehat{\omega} + K|^2} e^{\gamma \widehat{v}_{0\parallel}^2 K^2 / 4s|\widehat{\omega}+K|^4} , \tag{15}$$

The energy transport coefficient χ is defined as

$$\chi = \frac{\langle q_x \rangle}{-\frac{dP_0}{dx}} = \frac{L_n}{P_0(1+\eta_i)} \langle \tilde{v}_x^* \tilde{p} + \tilde{v}_x \tilde{p}^* \rangle = |\phi_0|^2 \frac{c^2 L_n |\widehat{\omega}| k_y (\pi\gamma)^{\frac{1}{2}}}{c_s B^2 \rho_s s^{\frac{5}{2}}} e^{\gamma \widehat{v}_{0\parallel}^2 K^2 / 4s|\widehat{\omega}+K|^4} . \tag{16}$$

The transport coefficients ($\mu_\perp$, $\mu_\parallel$, χ) are proportional to the square of the fluctuation level $\langle \tilde{\phi}^2 \rangle$. It is important to consider the ratio of the coefficients for which the dependence on $\tilde{\phi}$ is removed.

The ratios of the energy transport coefficient to the momentum transport coefficients are,

$$\frac{\chi}{\mu_\perp} = \frac{\gamma |\widehat{\omega} + K|^2}{|\widehat{\omega}|^2 K} \tag{17}$$

$$\frac{\chi}{\mu_\parallel} = \frac{|\widehat{\omega} + K|^2}{|\widehat{\omega}|^2} . \tag{18}$$

The ratios in Eqs. (17) and (18) are the reciprocal of the perpendicular and the parallel Prandtl numbers for the turbulent plasmas. The approximate solution for the dispersion

equation can be written as

$$\gamma \simeq \frac{sK}{1-\frac{\widehat{v}_{0\|}'^2}{4K}}\,, \tag{19}$$

if $\frac{1}{2}|\widehat{v}_{0\|}'| \lesssim sK$, which is generally true in tokamak plasmas nowadays. As a result, in this parameter regime we have

$$\frac{\chi}{\mu_\perp} \sim \frac{1-\frac{\widehat{v}_{0\|}'^2}{4K}}{s} + sK^2\,,$$

and

$$\frac{\chi}{\mu_\|} \sim \frac{\left(1-\frac{\widehat{v}_{0\|}'^2}{4K}\right)}{s^2} + 1\,.$$

The comparison with the Prandtl numbers for Coulomb collision plasma will be given in Sec. IV.

IV. Numerical Evaluation of the Transport Coefficients

The dispersion equation (2) is solved numerically. Typical mode growth rates and frequencies are shown in Fig. 1. The reference parameters are $s = 0.1$, $b_s = 0.1$, and $\tau = 1$. In Fig. 1(a) the mode growth rate is shown as function of $\widehat{v}_{0\|}' = L_n dv_\|/c_s dx$ for $\eta_i = 0.5$, 1.0, 1.5, and 2.0. It is clear in the figure that there are two regimes for the mode development. In the first regime, where $\widehat{v}_{0\|}' \lesssim 1$ and the growth of the mode is dominated by the ion temperature gradient, the mode growth rate increases slowly with $\widehat{v}_{0\|}'$. In the second regime, where $\widehat{v}_{0\|}' \gtrsim 2$ and the growth of the mode is dominated by the parallel velocity shear, the mode growth rate increases rapidly with $\widehat{v}_{0\|}'$. The approximate mode growth rate is given by Eq. (19) in the first regime. The higher the η_i value (deeper $T_i(r)$ profile or flatter density profile $n(r)$) or the lower the τ value (lower T_e or higher T_i), the flatter the curves γ versus $\widehat{v}_{0\|}'$.

In the second regime the approximate solution of the dispersion equation (2) is

$$\hat{\omega} = \frac{1}{2(1+b_s)} \left\{ 1 - is + \left[(1-is)^2 - (1+b_s)\hat{v}_{0\|}'^2 \left(1 - \frac{2K(1+b_s)^{\frac{1}{2}}}{i|\hat{v}_{0\|}'| + 1} \right) \right]^{\frac{1}{2}} \right\} , \qquad (20)$$

if K is small compared with $|\hat{v}_{0\|}'|$. For small magnetic shear Eq. (20) gives

$$\gamma \simeq \frac{1}{2(1+b_s)^{\frac{1}{2}}} \left(|\hat{v}_{0\|}'| - \frac{K+s}{|\hat{v}_{0\|}'|} \right) . \qquad (21)$$

The mode real frequency exhibits two flat regimes and a transition regime. The higher the η_i value the larger the difference between the two flat regimes. Generally speaking, the mode rotates in the ion diamagnetic direction and frequency increases with $\hat{v}_{0\|}'$. The frequency in the laboratory frame is Doppler shifted from what is given here where $v_\|(x=0) = 0$.

The micro-Reynolds stress π_{xy} without the factor $|\phi_0|^2 c^2/\rho_s B^2$ is plotted in Fig. 2 as function of x for $\eta_i = 1$, $\tau = 1$, $b_s = 0.1$. In Fig. 2(a) $s = 0.1$ and $\hat{v}_{0\|}' = -1.5$, -1.0, -0.5 and 0.0. It is easy to see that π_{xy} is antisymmetric about the $x = 0$ surface for $\hat{v}_{0\|}' = 0$ and that the asymmetry develops dramatically with the increasing of $|\hat{v}_{0\|}'|$. In addition, the magnitude of the micro-Reynolds stress π_{xy} increases significantly with $|\hat{v}_{0\|}'|$. In Fig. 2(b) $s = 0.5$ and $\hat{v}_{0\|}' = -1.5$, -0.5, 0.5, and 1.5. Comparison of the two cases with $\hat{v}_{0\|}' = -1.5$ shows that the asymmetry is higher while the amplitude is lower for $s = 0.5$ than that for $s = 0.1$.

The Reynolds stress $\langle \pi_{xy} \rangle$ (Eq. (11)) without the factor $|\phi_0|^2 c^2/\rho_s B^2$ is given in Fig. 3 as function of $\hat{v}_{0\|}'$ for $\tau = 1$, $b_s = 0.1$. In Fig. 3(a) $\eta_i = 1.0$, $s = 0.1$, 0.2, 0.3, and 0.4. It is shown that for the same $\hat{v}_{0\|}'$, $|\langle \pi_{xy} \rangle|$ decreases with the magnetic shear s, and that for all the s values studied here the Reynolds stress increases with the parallel velocity shear $|\hat{v}_{0\|}'|$. The sign of $\langle \pi_{xy} \rangle$ is opposite to the sign of $\hat{v}_{0\|}'$. In Fig. 3(b) $s = 1$, $\eta_i = 2$, 3, 4, and 5. It is seen that $|\langle \pi_{xy} \rangle|$ increases with the increasing of η_i for $\hat{v}_{0\|}' \lesssim 1.5$ where the ion temperature gradient is the dominant driving force. For $\hat{v}_{0\|}' \gtrsim 2$ it is the opposite, $|\langle \pi_{xy} \rangle|$ increases with the decreasing of η_i.

The micro-Reynolds stress $\pi_{x\|}$ without the factor $|\phi_0|^2 cc_s e/BT_e$ as function of x is plotted in Fig. 4 for $\tau = 1$, $b_s = 0.1$, $s = 0.1$. In Fig. 4(a) $\eta_i = 1$, $\widehat{v}'_{0\|} = -1.5,\ -1.0,\ -0.5$, and 0. Similar to π_{xy}, the stress $\pi_{x\|}$ is inversely symmetric about the $x = 0$ surface when $\widehat{v}'_{0\|} = 0$ and such symmetry breaks as long as $\widehat{v}'_{0\|} \neq 0$. In Fig. 4(b) $\widehat{v}'_{0\|} = -1.5$, $\eta_i = 1$, 2, 3, and 4. Both the amplitude and the asymmetry of $\pi_{x\|}(x)$ increase with parallel velocity shear $|\widehat{v}'_{0\|}|$ as well as with the ion temperature gradient η_i for the parameters studied here.

The Reynolds stress $\langle \pi_{x\|} \rangle$ (Eq. (12)) is plotted as function of parallel velocity shear $\widehat{v}'_{0\|}$ in Fig. 5 for $\tau = 1$, $b_s = 0.1$. In Fig. 5(a) $s = 0.1$, $\eta_i = 2$, 3, 4 and 5. The Reynolds stress $\langle \pi_{x\|} \rangle$ increases with the increasing of η_i for $|\widehat{v}'_{0\|}| \lesssim 1.5$. For $|\widehat{v}'_{0\|}| \gtrsim 2$ it decreases while η_i increases. In Fig. 5(b) $\eta_i = 3$, $s = 0.1$, 0.2, 0.3 and 0.4. The Reynolds stress $\langle \pi_{x\|} \rangle$ increases when the magnetic shear s decreases. For $\eta_i \sim 1$ the Reynolds stress $\langle \pi_{x\|} \rangle$ is not sensitive to the magnetic shear s. In addition, $\langle \pi_{x\|} \rangle$ has the opposite sign to the flow shear $\widehat{v}'_{0\|}$.

A common feature of $\langle \pi_{xy} \rangle$ and $\langle \pi_{x\|} \rangle$ is that both of them are equal to zero for $\widehat{v}'_{0\|} = 0$ and that the magnitudes increase with the increasing of the flow shear $\widehat{v}'_{0\|}$.

The micro-thermal flux q_x is given in Fig. 6 for $\tau = 1$, $b_s = 0.1$, and $s = 0.1$. In Fig. 6(a) $\widehat{v}'_{0\|} = -1.5$, $\eta_i = 1$, 2, 3, and 4. In contrast to the momentum fluxes π_{xy} and $\pi_{x\|}$, the energy flux is always positive and increases with η_i. In Fig. 6(b) $\eta_i = 1$, $\widehat{v}'_{0\|} = -1.5,\ -0.5,\ 0.5$, and 1.5. It is easy to notice that the curve for $\widehat{v}'_{0\|} = -1.5$ is identical to the curve for $\widehat{v}'_{0\|} = 1.5$ but shifts towards the left. It is the same for the curves of $\widehat{v}'_{0\|} = -0.5$ and 0.5.

The integrated energy flux $\langle q_x \rangle$ (Eq. (13)) is shown in Fig. 7 as function of the parallel flow shear $\widehat{v}'_{0\|}$ for $\tau = 1$, $b_s = 0.1$. For given magnetic shear $s = 0.1$ the energy flux increases with the increasing of η_i (see Fig. 7(a)) while for $\eta_i = 1$ it decreases with the increasing of the magnetic shear s (see Fig. 7(b)). The momentum fluxes $\langle \pi_{xy} \rangle$ and $\langle \pi_{x\|} \rangle$ are zero while the energy flux is not for $\widehat{v}'_{0\|} = 0$.

All the above mentioned variations of $\langle \pi_{xy} \rangle$, π_{xy}, $\langle \pi_{x\|} \rangle$, $\pi_{x\|}$, $\langle q_x \rangle$ and q_x with the parameters $(s, \eta_i\ , \widehat{v}_{0\|})$ are like at a fixed ϕ_0^2 so that additional variation through the dependence of

ϕ_0^2 on the parameters must be calculated by other means in a comparison with a real physics system.

The ratio of the energy transport coefficient χ over the poloidal momentum transport coefficient $\mu_\perp$ (the inverse Prandtl number) is independent of ϕ_0^2 and given in Fig. 8 as function of $\widehat{v}'_{0\|}$ for $\tau = 1$, $s = 0.1$. In Fig. 8(a) $b_s = 0.1$, $\eta_i = 1$, 2, 3, and 4. One interesting point of the result is that $\chi/\mu_\perp$ decreases when η_i increases for $|\widehat{v}'_{0\|}| \lesssim 1$ while it is the opposite for $|\widehat{v}'_{0\|}| \gtrsim 1.5$: lower η_i corresponds to lower $\chi/\mu_\perp$. In Fig. 8(b) $\eta_i = 1$, $b_s = 0.1$, 0.2, 0.3, and 0.4. The ratio $\chi/\mu_\perp$ monotonously decreases for increasing b_s. Not shown here is the results we obtained that $\chi/\mu_\perp$ monotonously increases for decreasing magnetic shear s. The common feature is that χ and $\mu_\perp$ are always positive and the value $\chi/\mu_\perp$ decreases with the increasing of the parallel flow shear $|\widehat{v}'_{0\|}|$.

Figure 9 shows the inverse Prandtl number defined with respect to the parallel turbulent viscosity $\chi/\mu_\|$. The results are similar except that $\chi/\mu_\|$ is more than one order of magnitude higher than $\chi/\mu_\perp$, which means that $\mu_\perp$ is much higher than $\mu_\|$.

For Coulomb collisions the corresponding inverse Prandtl numbers are

$$\frac{\chi}{\mu_1} \simeq 7\,, \qquad \frac{\chi}{\mu_2} \simeq 1.7\,.$$

Here μ_2 corresponds to $\mu_\|$ in the turbulence case and μ_1 is perpendicular viscosity coefficient with no direct correspondence to the turbulent viscosities given here. Thus the turbulent Prandtl numbers ($\simeq 0.01$) are small compared with the Coulomb collisional values ($\simeq 0.6$). There are no parameters in the theory based on the Coulomb collision corresponding to $\mu_\perp$. The parameter $\mu_\perp$ introduced in this work is unique for the theory of turbulence driven by velocity shear.

V. Discussion

It is widely recognized by fusion physicists[18,23,24] that the plasma dynamics in the bulk region and in the scrape off layer (SOL) are significantly different from each other. As a consequence there must be a transition region around the edge of the limiter or the last closed flux surface (LCFS), where some of the plasma parameters change rather rapidly across the region. In other words, the edge plasma is characterized by a rapid radial dependence of the plasma parameters such as parallel plasma flow. Particles may move freely along the magnetic field lines in the bulk plasma while such freedom does not exist in SOL due to the presence of limiter or divertor plates.

Experimentally, a poloidal flow shear has been observed in the vicinity of a material limiter,[10] in a ohmically heated plasma. The poloidal velocity shear is important in the L-H transition.[11] We present evidence that the plasma parallel velocity changes at about the same radial location as the poloidal shear flow layer. These measurements were taken on the TEXT-U tokamak with plasma conditions $B_T = 2.5\,\mathrm{T}$, $I_p = 220\,\mathrm{kA}$, and a line averaged density, $\overline{n}_e = 3.0 \times 10^{13}\,\mathrm{cm}^{-3}$, using a reciprocating probe array. The plasma was defined by three rail limiters located at $r = 27\,\mathrm{cm}$. The probe array was mounted on the top of the vessel separated from the limiters by 247.5° in the plasma current direction. The toroidal magnetic field was in the same direction as the plasma current, and the ion grad-B drift was upwards. In Fig. 10(a) we show a radial profile of the parallel flow Mach number $M = v_{\|}/c_s$ measured with a Mach probe with two collecting electrodes biased with $-180\,\mathrm{V}$ to collect ion saturation currents from upstream and downstream. The current ratio can then be used to calculate the flow Mach number[25–27] with the assumption that the ion temperature is equal to the electron temperature. We used the Hutchinson model[27] which includes diffusion and viscosity into the probe presheath. The ion flow direction is in the direction of the toroidal magnetic field and plasma current. Figure 10(b) presents the normalized radial derivative of the ion parallel

velocity. In Fig. 10(c) we show a radial profile of the poloidal phase velocity, $v_{\rm phase}$, used to define the shear layer.[10] The phase velocity is derived from the power spectrum measured with a two point correlation technique, $v_{\rm phase} = \sum_{k,\omega} \frac{\omega}{k} S(\omega,k) / \sum_{k,\omega} S(\omega,k)$, where $S(k,\omega)$ is the measured power spectra[28] as a function of wavenumber and frequency. Since the phase velocity measurements were not taken on the same shot as the data on parallel flow velocity, it is important to note that the conditions were similar and the location of the velocity shear layer is generally robust for the plasma conditions used. We estimate the uncertainty in position for the location of the flow shear layer to be of order 4 mm. To within the limits of plasma reproducibility the maximum gradient of the parallel ion flow occurs at the same radial position as the velocity shear in the perpendicular direction.

In order to make detailed comparison possible the quasilinear saturation amplitude is estimated in the following. Suppose that the mixing length saturation level is determined by the condition that

$$x \frac{dv_\parallel}{dx} \sim \tilde{v}_\parallel(x) \ , \tag{22}$$

which is valid if $|\widehat{v}'_{0\parallel}| \gtrsim 1 + \eta_i$. Noting from the motion equation in the parallel direction that $\tilde{v}_\parallel = (esc_s/T_e\widehat{\omega}) x \tilde{\phi}$ then it is straightforward to have

$$\phi_0 \sim \frac{T_e}{e} \frac{\rho_s}{L_n} \widehat{v}'_{0\parallel} \ . \tag{23}$$

For $\widehat{v}'_{0\parallel} < 1 + \eta_i$ the saturation level is $\phi_0 \simeq (\eta_i - \eta_{ic}) / \langle k_x^2 \rangle^{\frac{1}{2}} \simeq (\eta_i - \eta_{ic}) / \langle k_y^2 \rangle^{\frac{1}{2}}$.

Substituting Eq. (23) into Eqs. (11)–(13) gives the approximate formulas as follows

$$\begin{aligned} \langle \pi_{xy} \rangle &= -\frac{c^2 T_e^2}{e^2 B^2 L_n^2} \frac{(\pi)^{\frac{1}{2}} k_y \rho_s}{s^{\frac{5}{2}}} \frac{\gamma^{\frac{1}{2}} |\widehat{\omega}|^2 K \widehat{v}'^3_{0\parallel}}{|\widehat{\omega} + K|^2} \\ &= -\left(\frac{cT_e}{eBL_n}\right)^2 F_\perp(\eta_i, \tau, s, \widehat{v}'_{0\parallel}, b_s) \ , \end{aligned} \tag{24}$$

$$\langle \pi_{x\parallel} \rangle = -\frac{c^2 T_e^2}{e^2 B^2 L_n^2} \frac{(\pi)^{\frac{1}{2}} k_y \rho_s}{s^{\frac{5}{2}}} \frac{\gamma^{\frac{1}{2}} |\widehat{\omega}|^3 \widehat{v}'^3_{0\parallel}}{|\widehat{\omega} + K|^2}$$

$$= -\left(\frac{cT_e}{eBL_n}\right)^2 F_{\parallel}(\eta_i, \tau, s, \widehat{v}'_{0\parallel}, b_s) \ , \tag{25}$$

$$\langle q_x \rangle = \frac{c^2 T_e^2}{e^2 B^2 L_n c_s} \frac{P_0(1+\eta_i)(\pi\gamma)^{\frac{1}{2}} k_y \rho_s}{L_n s^{\frac{5}{2}}} |\widehat{\omega}| \widehat{v}'^2_{0\parallel}$$

$$= -\left(\frac{\rho_s^2 c_s}{L_n}\right) G(\eta_i, \tau, s, \widehat{v}'_{0\parallel}, b_s) \frac{dP_0}{dx} \ . \tag{26}$$

To obtain the fluxes as function of system parameters the value of $\widehat{\omega} = \widehat{\omega}_r + i\gamma$ must be calculated from Eq. (2) and substitute into Eqs. (24)–(26).

The dimensionless functions $F_{\perp}$, $F_{\parallel}$, and G are given by

$$F_{\perp}(\eta_i, \tau, s, \widehat{v}'_{0\parallel}, b_s) = \frac{(\pi)^{\frac{1}{2}} k_y \rho_s}{s^{\frac{5}{2}}} \frac{\gamma^{\frac{1}{2}} |\widehat{\omega}|^2 K \widehat{v}'^3_{0\parallel}}{|\widehat{\omega} + K|^2} \ ,$$

$$F_{\parallel}(\eta_i, \tau, s, \widehat{v}'_{0\parallel}, b_s) = \frac{(\pi)^{\frac{1}{2}} k_y \rho_s}{s^{\frac{5}{2}}} \frac{\gamma^{\frac{1}{2}} |\widehat{\omega}|^3 \widehat{v}'^3_{0\parallel}}{|\widehat{\omega} + K|^2} \ ,$$

and

$$G(\eta_i, \tau, s, \widehat{v}'_{0\parallel}, b_s) = \frac{(\pi\gamma)^{\frac{1}{2}} k_y \rho_s}{s^{\frac{5}{2}}} |\widehat{\omega}| \widehat{v}'^2_{0\parallel} \ .$$

The equation for generation of the poloidal velocity $\langle v_\theta \rangle$ is

$$\frac{\partial}{\partial t} \langle v_\theta \rangle = -\frac{1}{r} \frac{\partial}{\partial r} (r \langle \pi_{xy} \rangle) \ . \tag{27}$$

In our case, suppose that the parameters are constant except $\widehat{v}'_{0\parallel}$, then

$$\frac{\partial}{\partial x} \langle \pi_{xy} \rangle = -\frac{c^2 T_e^2}{e^2 L_n^3 B^2} \frac{k_y \rho_s (\pi)^{\frac{1}{2}}}{s^{\frac{5}{2}}} \frac{\gamma^{\frac{1}{2}} |\widehat{\omega}|^2 K}{|\widehat{\omega} + K|^2} \left(3 + \frac{\gamma K^2 \widehat{v}'^2_{0\parallel}}{2s|\widehat{\omega} + K|^4}\right) \widehat{v}'^2_{0\parallel} \widehat{v}''_{0\parallel}$$

$$= -\frac{c^2 T_e^2}{e^2 L_n^3 B^2} H(\eta_i, \tau, s, b_s, \widehat{v}'_{0\parallel}, \widehat{v}''_{0\parallel}) \ , \tag{28}$$

where $\widehat{v}''_{0\parallel} = L_n^2 d^2 v_{\parallel} / c_s dx^2$ and

$$H(\eta_i, \tau, s, b_s, \widehat{v}'_{0\parallel}, \widehat{v}''_{0\parallel}) = \frac{k_y \rho_s (\pi)^{\frac{1}{2}}}{s^{\frac{5}{2}}} \frac{\gamma^{\frac{1}{2}} |\widehat{\omega}|^2 K}{|\widehat{\omega} + K|^2} \left(3 + \frac{\gamma K^2 \widehat{v}'^2_{0\parallel}}{2s|\widehat{\omega} + K|^4}\right) \widehat{v}'^2_{0\parallel} \widehat{v}''_{0\parallel} \ .$$

Equations (27) and (28) clearly show that the driving force for the poloidal velocity is independent of the sign of $\widehat{v}'_{0\|}$ but depends on the sign of $\widehat{v}''_{0\|}$. Such dependence of the driving force on $\widehat{v}''_{0\|}$ determines the dependence of $\langle v_\theta \rangle$ on $\widehat{v}''_{0\|}$ and will be discussed later. In general, the functions $F_\perp$, $F_\|$, G, and H should be replaced by $F_\perp A$, $F_\| A$, GA, and HA, where the exponential part $A = \exp(\gamma \widehat{v}'^2_{0\|} K^2/4s|\widehat{\omega} + K|^4) \sim 1$ since for a real system $\gamma \widehat{v}'^2_{0\|} K^2/4s|\widehat{\omega} + K|^4 \simeq \gamma \widehat{v}'^2_{0\|}/4sK^2 \ll 1$ when γ is given by Eq. (19).

Measurements from the TEXT-U experiment show[29] that the measured poloidal plasma velocity shear increases with plasma current, decreases with chord average density and the toroidal magnetic field. The shear layer width is a constant over a range of discharge conditions. There is no explicit dependence on plasma density $\overline{n}$ and current I_p in Eq. (28). However, both the decrease of density $\overline{n}$ and the increase of current I_p correspond to an increase of electron temperature T_e in the shear layer which explicitly appears in Eq. (28). The poloidal driving force given in Eq. (28) is inversely proportional to B^2. In summary, the driving force given in Eq. (28) is qualitatively in agreement with the measured scaling if the damping mechanism is approximately independent of those parameters. There is no simple scaling for the shear layer width from this model. Physically, it is reasonable to think that the poloidal shear layer width is approximately the same as of the parallel flow shear.

Some damping mechanism must be introduced to estimate the steady state poloidal velocity driven by the turbulence. As an example the magnetic damping is considered as the only damping mechanism and equilibrium poloidal velocity is included. Under these conditions the plasma motion equation in the poloidal direction, Eq. (27) will be modified as follows,[6,17,20]

$$\frac{\partial}{\partial t}\langle v_\theta \rangle = -\frac{1}{r}\frac{\partial}{\partial r}\left(r\langle \pi_{xy} \rangle\right) - \nu^{nc}\left(\langle v_\theta \rangle - v_\theta^{nc}\right) , \tag{29}$$

where v_θ^{nc} is the equilibrium poloidal velocity, and

$$\nu^{nc} = \frac{\nu_{ii}}{\epsilon^{\frac{3}{2}}(1+\nu_*)(1+\epsilon^{\frac{3}{2}}\nu_*)} , \tag{30}$$

with $\nu_* = \nu_{ii} qR/v_{th}\epsilon^{\frac{3}{2}}$ and ϵ is the inverse aspect ratio, q the safety factor, R the major radius and ν_{ii} the ion-ion collision frequency. In steady state Eq. (29) reduces to

$$\langle v_\theta \rangle - v_\theta^{nc} = -\frac{1}{\nu^{nc}} \frac{\partial}{\partial x} \langle \pi_{xy} \rangle \ . \tag{31}$$

For the dimensionless parameters (η_i, s, τ, $\hat{v}'_{0\|}, b_s$) of order unity the poloidal acceleration from the divergence of the momentum flux is of the magnitude $(cT_e/eBL_n)^2/L_n \simeq v_{de}^2/L_n$ compared with the neoclassical damping rate ν^{nc}.

In order to make further comparison it is assumed that the equilibrium poloidal velocity v_θ^{nc} is negligible, and that the plasma is around the boundary between the Pfirsch-Schlüter and the plateau regimes with $l \sim qR$ so that $\nu^{nc} \simeq \nu_{ii}$. Then the steady state poloidal velocity (Eq. (31)) reduces to

$$\langle v_\theta \rangle = \frac{1}{\nu_{ii}} \frac{v_{de}^2}{L_n} H(\eta_i, \tau, s, b_s, \hat{v}'_{0\|}, \hat{v}''_{0\|}) \ . \tag{32}$$

For the typical discharge parameters: $T_e = T_i = 40\,\text{ev}$, $B = 20\,\text{kG}$, $n = 3 \times 10^{12}/\text{cm}^3$, $L_n = 3\,\text{cm}$, it turns out that

$$\frac{1}{\nu_{ii}} \frac{v_{de}^2}{L_n} \simeq 2.1 \times 10^5\,\text{cm/s} \ .$$

The function H is sensitive to $\hat{v}'_{0\|}$. For the parameters used in this study, i.e. $s = 0.1$, $b_s = 0.1$, $\eta_i \sim 1$, $\tau = 1$, the results are given in Fig. 11. H versus $\hat{v}''_{0\|}$ is given in Fig. 11(a) for $\hat{v}'_{0\|} = 0.5$. The maximum value of H is about 10 for $\hat{v}'_{0\|} = 1$. These numbers are in reasonable agreement with the experimental observations, $\langle v_\theta \rangle \sim -3$ to $+3 \times 10^5\,\text{cm/s}$. It should be noted that the suppression effect of the poloidal velocity shear on the fluctuation is not considered in this work. In this regard the driving force from the turbulent Reynolds stress is overestimated. On the other hand, however, the saturation level evaluation (Eq. (23)) is made without taking the ion temperature gradient (η_i) effect into account. This may lead to underestimation of the driving force. These two factors may compensate each other so that the theoretical numbers are well in the regime of the experimental observations.

According to Eq. (32) the dependence of $\langle v_\theta \rangle$ on $\widehat{v}''_{0\|}$ is the same as given in Eq. (28) for the driving force and is qualitatively in agreement with the experimental observations given in Fig. 10 from TEXT-U tokamak. Roughly speaking, $\langle v_\theta \rangle$ has the same sign as that of $\widehat{v}''_{0\|}$ and changes sign at the same location where $\widehat{v}''_{0\|} \simeq 0$. The correlation between $\langle v_\theta \rangle$ and $\widehat{v}''_{0\|}$ is very impressive though the data shown here are not from same discharge. To further study the profile of the turbulence driven $\langle v_\theta \rangle$, the profile of the derivative of the parallel velocity can be modeled as $\widehat{v}'_{0\|}(x) = -0.5\,\mathrm{sech}(\alpha x)$, with α being a constant of order unity and $x = 0$ the position where $\widehat{v}'_{0\|}(x)$ has minimum. Then the function $H(x)$ is given in Fig. 11(b). It is reasonable to assume that $v_{de}^2/\nu_{ii}L_n$ is roughly a constant in the velocity shear layer. Under these assumptions the poloidal velocity profile from this model is approximately the same as that given in Fig. 11(b) which is similar to the experimental results given in Fig. 10(c) and Ref. 29.

The width of the velocity shear layer can be estimated as

$$\Delta \simeq \frac{\langle \pi_{xy} \rangle}{\nu_{ii}\langle v_\theta \rangle} \sim \frac{4 \times 10^9}{3.2 \times 10^9} \sim 1 \text{ cm} \tag{33}$$

and is in good agreement with the experimental observations.

To close this section we would like to say a few words about the L-H transition from the point of view of the model suggested in this work. One typical feature of the L-H transition is that v_θ and $|v'_\theta| = |dv_\theta/dr|$ increase very rapidly ($\sim 100\mu s$) during the transition. The driving force given in Eq. (28) exponentially increases with $\widehat{v}'^2_{0\|}K^2/|\widehat{\omega} + K|^4$. Usually $|\widehat{\omega}| < K$ so that such increase is slow as long as $|\widehat{v}'_{0\|}| < K$. However, the acceleration increases very rapidly when $|\widehat{v}'_{0\|}| \gtrsim K$. It may be possible that the condition $|\widehat{v}'_{0\|}| \gtrsim K$, (i.e. $|v_\|/dx| \gtrsim c_s(L_n + L_T)T_i/L_nL_TT_e$,) somehow is achieved and triggers the L-H transition. Another concern is how the acceleration process is stopped. It has been demonstrated[2–4,12] that the mode growth rate will decrease after the poloidal flow is driven up. The driving force in Eq. (28) is proportional to the $\frac{3}{2}$-power of the mode growth rate so that the acceleration

stops when the mode becomes marginally stable. This stopping effect can be modelled by taking $\gamma = \gamma_0(1 - v_\theta'^2/v_{\theta\text{crit}}'^2)$. Another mechanism to stop the acceleration is that L_n becomes very small in the shear flow layer after L-H transition so that the dimensionless driving force parameter $\widehat{v}_{0\|}' = L_n dv_\|/c_s dr$ is negligibly small even though $dv_\|/dr$ does not change very much. Of course, the plasma will eventually enter into a steady state if other drag forces such as the magnetic damping are taken into account.

VI. Conclusions

The instability driven by parallel flow shear is studied within the fluid approximation in a local slab configuration with magnetic shear. Ion temperature gradient η_i is taken into account. The dimensionless parameter set of the problem is $(\eta_i, \tau, s, \widehat{v}_{0\|}', b_s)$. The quasilinear expressions for the radial fluxes of the parallel momentum $\langle \pi_{x\|} \rangle$, the perpendicular momentum $\langle \pi_{xy} \rangle$ and the thermal energy $\langle q_x \rangle$ are derived using the exact linear eigenfunction. The perpendicular and parallel momentum fluxes, called Reynolds stress, are shown to vanish when the dimensionless parameter $\widehat{v}_{0\|}' = 0$ due to the symmetry feature of the mode structure about the rational surface. Such symmetry property is broken leading to nonzero parallel and perpendicular momentum transport as long as $\widehat{v}_{0\|}' \neq 0$. This dependence on the parallel velocity shear does not hold for the thermal energy flux: $\langle q_x \rangle$ does not vanish when $\widehat{v}_{0\|}' = 0$. The Reynolds stress exponentially increases with $(T_e L_n L_T/T_i(L_n + L_T)c_s)^2(dv_\|/dx)^2$, while it is proportional to the square of the electron temperature T_e^2 and inversely proportional to the square of the toroidal magnetic field B^2. Experimental measurements of the parallel and poloidal plasma flows on TEXT-U tokamak are carried out and the results support the interpretation that the poloidal shear flow is generated through the turbulence driven by parallel sheared plasma flow. The theoretical models are compared and shown to be of reasonable agreement with the experimental observations for scalings as well as for magnitudes when the neoclassical damping mechanism is introduced to balance the driving force from

the Reynolds stress.

The transport coefficients $(\mu_\perp, \mu_\parallel, \chi)$ induced by the $\mathbf{E} \times \mathbf{B}$ turbulence of the instability are obtained analytically. They are always positive. The positivity of the turbulent transport means that entropy production from the transformation of the ordered flows into the turbulent fluctuations is positive definite. The ratio of the energy transport coefficient to the viscosity coefficient is obtained and studied numerically.

The suppression effects of the poloidal velocity gradient on the fluctuations are not considered in this work. In Ref. 6 2D hydrodynamic simulations show the evolution of $\widehat{v}'_\parallel$-driven turbulence and the reaction of the turbulence through π_{xy} and π_{xy} on the mean shear flows including the creation of $\mathbf{E} \times \mathbf{B}$ shear flow. A self-consistent study about the poloidal flow generation by the turbulence and the fluctuation suppression by the poloidal velocity shear is in progress and will be published in a separate work.

As is pointed out in Ref. 23 that the tokamak plasma is a complex physical system. The edge region, where more physics processes take place than in the bulk region, is the most complex subsystem . The model suggested in this work does not exclude other models for the subject of the sheared flow generation. The parallel flow shear is only one of the physical phenomena which exhibit and influence the plasma behavior in the edge region. The emphasis here is that a parallel velocity shear does exist in the edge region and provide a free energy source for turbulence, as well as a symmetry breaking element which is necessary for the poloidal sheared flow generation by turbulence in the quasilinear theory.

Acknowledgments

The authors acknowledge useful discussions with T. Tajima. This work was supported by the U.S. Department of Energy contracts DE-FG05-80ET-53088 and DE-FG05-88ER-53267.

References

1. P.J. Catto, M.N. Rosenbluth, and C.S. Liu, Phys. Fluids **16**, 1719 (1973).

2. M. Artun and W.M. Tang, Phys. Fluids B **4**, 1102 (1992).

3. F.L. Waelbroeck, T.M. Antonsen, Jr. P.N. Guzdar, and A.B. Hassam, Phys. Fluids B **4**, 2441 (1992).

4. J.Q. Dong and W. Horton, Phys. Fluids B **5**, 1581 (1993).

5. D.R. McCarthy, J.F. Drake, and P.N. Guzdar, Phys. Fluids B **5**, 2145 (1993).

6. X.N. Su, P.N. Yushmanov, J.Q. Dong, and W. Horton, Phys. Plasmas **1**, 1905 (1994).

7. S. Migliuolo, J. Geophys. Res. **93**, 867 (1988).

8. W. Horton, J.Q. Dong, X.N. Su, and T. Tajima, J. Geophys. Res. **98**, 13377 (1993).

9. D. Schriver and M. Ashour-Abdalla, J. Geophys. Res. **95**, 3987 (1990).

10. Ch.P. Ritz, R.D. Bengtson, S.J. Levinson, and E.J. Powers, Phys. Fluids. **27**, 2956 (1984).

11. R.J. Groebner, K.H. Burrell, and R.P. Seraydarian, Phys. Rev. Lett. **64**, 3015 (1990); R.J. Groebner, Phys. Fluids B **5**, 2343 (1993).

12. S. Hamaguchi and W. Horton, Phys. Fluids B **4**, 319 (1992).

13. K.C. Shaing and E.C. Crume, Jr., Phys. Rev. Lett. **63**, 2369 (1989).

14. R.D. Hazeltine, H. Xiao, and P. Valanju, Phys. Fluids B **5**, 4011 (1993).

15. P.H. Diamond and Y.B. Kim, Phys. Fluids B **3**, 1626 (1991).

16. B.A. Carreras, L. Garcia, and V.E. Lynch, Phys. Fluids B **3**, 1438 (1991).

17. A.B. Hassam, T.M. Antonsen, Jr., J.F. Drake, and C.S. Liu, Phys. Rev. Lett. **66**, 309 (1991).

18. H.Y.W. Tsui, Phys. Fluids B 4, 4057 (1992).

19. P.N. Guzdar, J.F. Drake, D. McCarthy, A.B. Hassam, and C.S. Liu, Phys. Fluids B **5**, 3712 (1993).

20. B.A. Carreras and V.E. Lynch, Phys. Fluids B **5**, 1491 (1993).

21. Y. Koide, M. Kikuchi, M. Mori, S. Tsuji, S. Ishida, N. Asakura, Y. Kamada, T. Nishitani, Y. Kawano, T. Hatae, T. Fujita, T. Fukuda, A. Sakasai, T. Kondoh, R. Yoshino, and Y. Neyatani, Phys. Rev. Lett. **72**, 3662 (1994).

22. A.D. Beklemishev and W. Horton, Phys. Fluids B 4, 2176 (1992).

23. B.B. Kadomtsev, *Tokamak Plasma: A Complex Physical System*, (IOP Publishing Ltd., 1992) p. 63.

24. X.Q. Xu, M.N. Rosenbluth, and P.H. Diamond, Phys. Fluids B **5**, 2206 (1993).

25. P.C. Stangeby, Phys. Fluids **27**, 682 (1984).

26. P.C. Stangeby, J. Nucl. Mater. **121**, 36 (1984).

27. I.H. Hutchinson, Phys. Fluids **30**, 3777 (1987).

28. J.M. Beall, Y.C. Kim, and E.J. Powers, J. Appl. Phys. **53**, 3933 (1982).

29. H. Lin, "Turbulence and transport studies in the edge plasma of the TEXT tokamak," Dissertation, The Univ. of Texas at Austin, October, 1991.

Figure Captions

1. (a) Normalized mode growth rate γ/ω_{*e} and (b) the real frequency ω_r/ω_{*e} vs. parallel flow shear $\widehat{v}'_{0\|} = L_n dv_\|/c_s dx$ for $s = 0.1$, $b_s = 0.1$, $\tau = 1$, $\eta_i = 0.5$, 1.0, 1.5, and 2.0.

2. Micro-Reynolds stress distribution π_{xy} around the mode rational surface $x = 0$ for $\eta_i = 1$, $\tau = 1$, $b_s = 0.1$ and (a) $s = 0.1$, $\widehat{v}'_{0\|} = -1.5,\ -1.0,\ -0.5$, and 0.0; (b) $s = 0.5$, $\widehat{v}'_{0\|} = -1.5,\ -0.5$, 0.5, and 1.5.

3. Reynolds stress $\langle \pi_{xy} \rangle$ vs. $\widehat{v}'_{0\|} = L_n dv_\|/c_s dx$ for $b_s = 0.1$, $\tau = 1$, and (a) $\eta_i = 1$, $s = 0.1$, 0.2, 0.3, and 0.4; (b) $s = 0.1$, $\eta_i = 2$, 3, 4, and 5.

4. Micro-Reynolds stress distribution $\pi_{x\|}$ around the mode rational surface $x = 0$ for $\tau = 1$, $b_s = 0.1$, $s = 0.1$ and (a) $\eta_i = 1$, $\widehat{v}'_{0\|} = -1.5,\ -1.0,\ -0.5$, and 0.0; (b) $\widehat{v}'_{0\|} = -1.5$, $\eta_i = 1$, 2, 3, and 4.

5. Reynolds stress $\langle \pi_{x\|} \rangle$ vs. $\widehat{v}'_{0\|} = L_n dv_\|/c_s dx$ for $b_s = 0.1$, $\tau = 1$, and (a) $s = 0.1$, $\eta_i = 2$, 3, 4, and 5; (b) $\eta_i = 3$, $s = 0.1$, 0.2, 0.3 and 0.4.

6. Energy flux distribution q_x around the mode rational surface $x = 0$ for $\tau = 1$, $b_s = 0.1$, $s = 0.1$ and (a) $\widehat{v}'_{0\|} = -1.5$, $\eta_i = 1$, 2, 3, and 4; (b) $\eta_i = 1$, $\widehat{v}'_{0\|} = -1.5,\ -0.5$, 0.5, and 1.5.

7. Energy flux $\langle q_x \rangle$ vs. $\widehat{v}'_{0\|} = L_n dv_\|/c_s dx$ for $b_s = 0.1$, $\tau = 1$, and (a) $s = 0.1$, $\eta_i = 2$, 3, 4, and 5; (b) $\eta_i = 1$, $s = 0.1$, 0.2, 0.3 and 0.4.

8. The ratio of the energy transport coefficient χ to the perpendicular viscosity coefficient $\mu_\perp$ vs. $\widehat{v}'_{0\|} = L_n dv_\|/c_s dx$ for $s = 0.1$, $\tau = 1$, and (a) $b_s = 0.1$, $\eta_i = 2$, 3, 4, and 5; (b) $\eta_i = 1$, $b_s = 0.1$, 0.2, 0.3 and 0.4.

9. The ratio of the energy transport coefficient χ to the parallel viscosity coefficient $\mu_{\|}$ vs. $\widehat{v}'_{0\|} = L_n dv_{\|}/c_s dx$ for $s = 0.1$, $\tau = 1$, and (a) $b_s = 0.1$, $\eta_i = 2$, 3, 4 and 5; (b) $\eta_i = 1$, $b_s = 0.1$, 0.2, 0.3 and 0.4.

10. The profile of (a) Mach number and (b) $\widehat{v}'_{0\|} = L_n dv_{\|}/c_s dx$ measured at the plasma edge in TEXT-U tokamak. (c) The poloidal velocity profile in a discharge of TEXT-U with $I_p = 160\,\mathrm{kA}$, $B_T = 2.2\,\mathrm{T}$ and $\overline{n}_e = 1.5 \times 10^{13}\,\mathrm{cm}^{-3}$.

11. (a) H vs. $\widehat{v}''_{0\|} = L_n^2 d^2 v_{\|}/c_s dx^2$ for $s = 0.1$, $b_s = 0.1$, $\tau = 1$, $\widehat{v}'_{0\|} = 0.5$ and $\eta_i = 1$, 1.1, 1.2, 1.3; (b) the modeling result for profile $H(x)$ which is roughly the same as profile $\langle v_\theta(x) \rangle$.

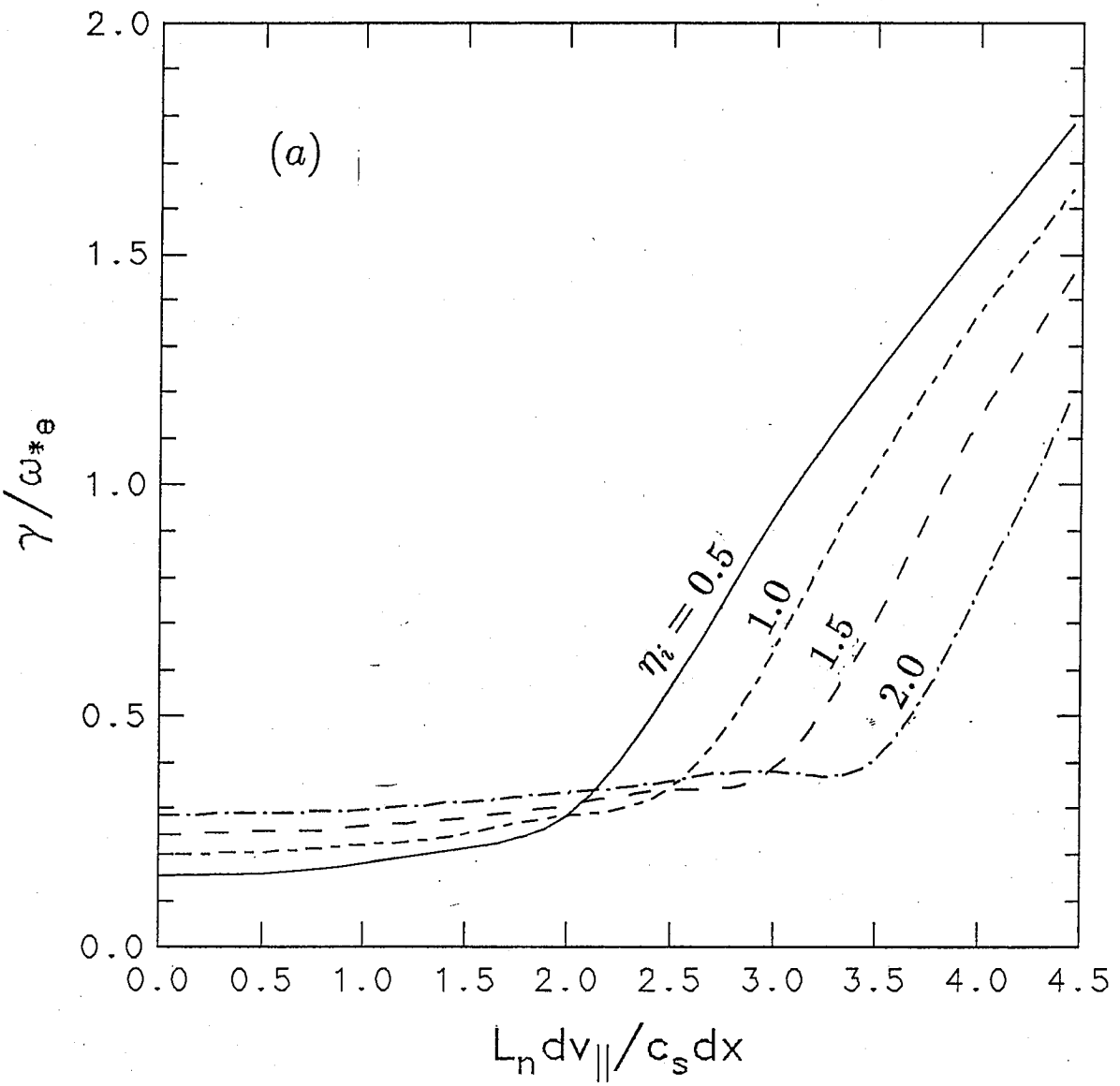
(a)
2.0
1.5
1.0
0.5
0.0
γ/ω_{*e}
$n_i = 0.5$
1.0
1.5
2.0
0.0 0.5 1.0 1.5 2.0 2.5 3.0 3.5 4.0 4.5
$L_n dv_{||}/c_s dx$

Fig. 1

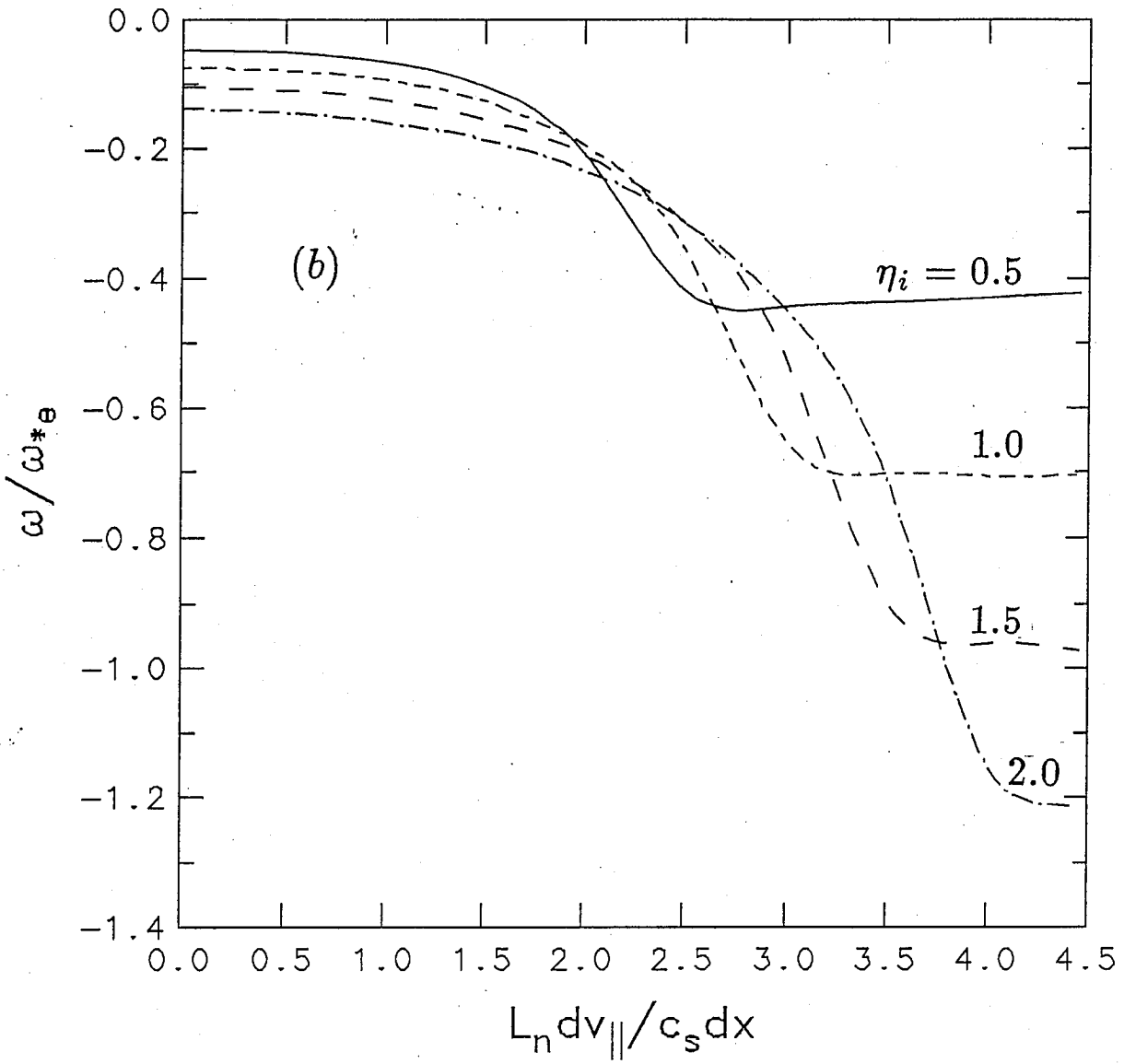
0.0
−0.2
−0.4
−0.6
−0.8
−1.0
−1.2
−1.4
0.0 0.5 1.0 1.5 2.0 2.5 3.0 3.5 4.0 4.5
ω/ω_{*e}
$L_n dv_{||}/c_s dx$
(b)
$\eta_i = 0.5$
1.0
1.5
2.0

Fig. 1

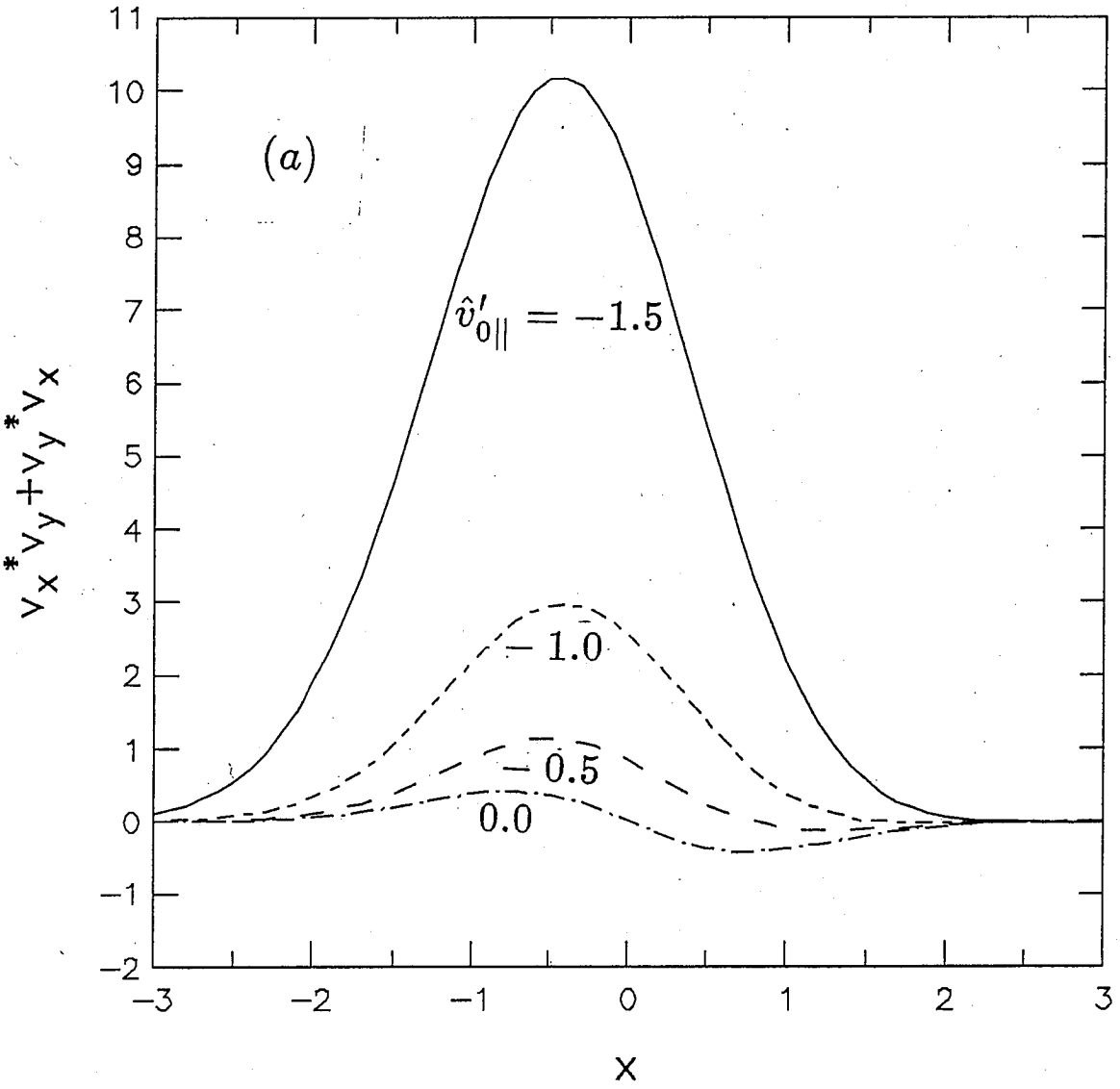

Fig. 2

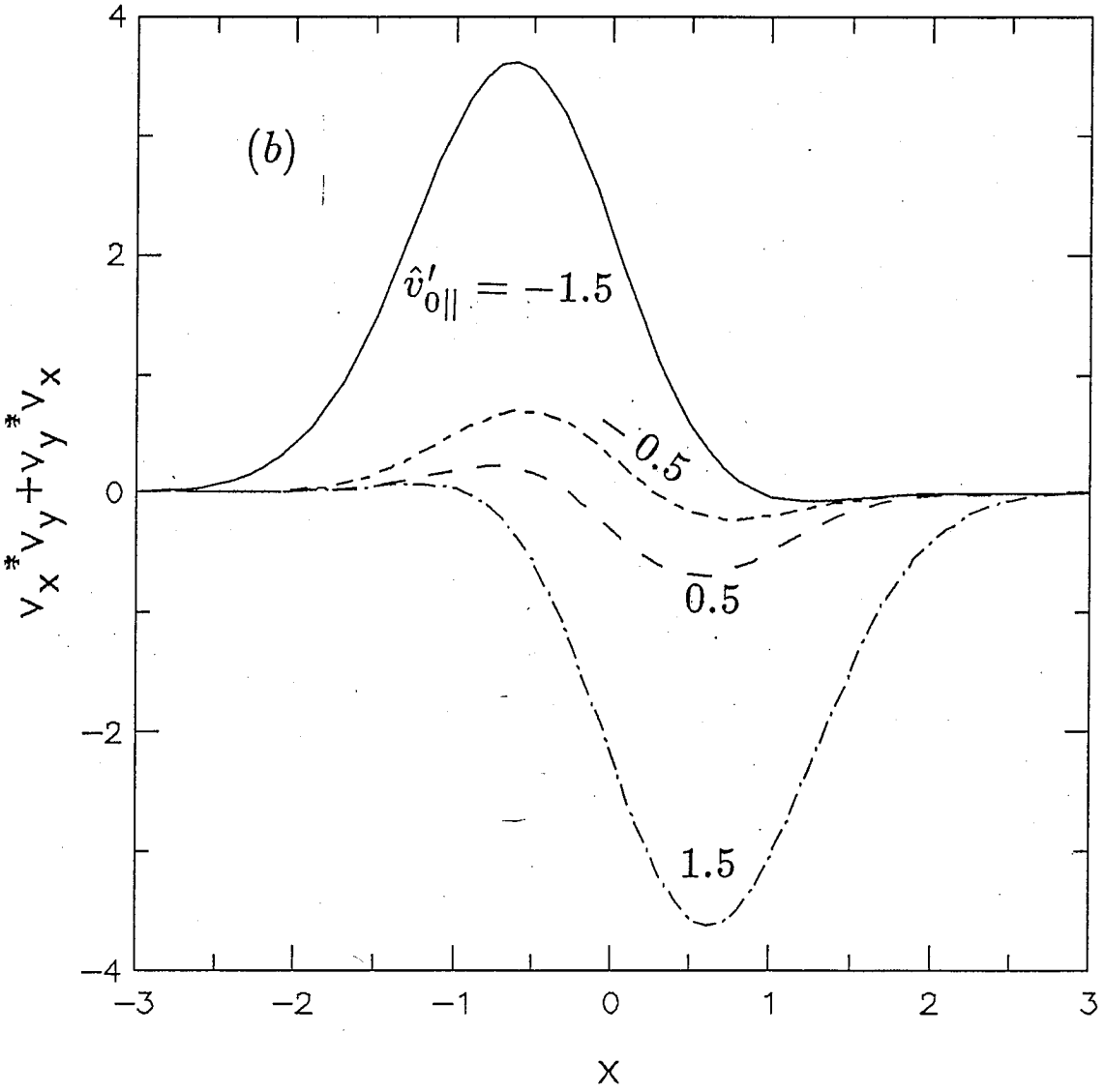

Fig. 2

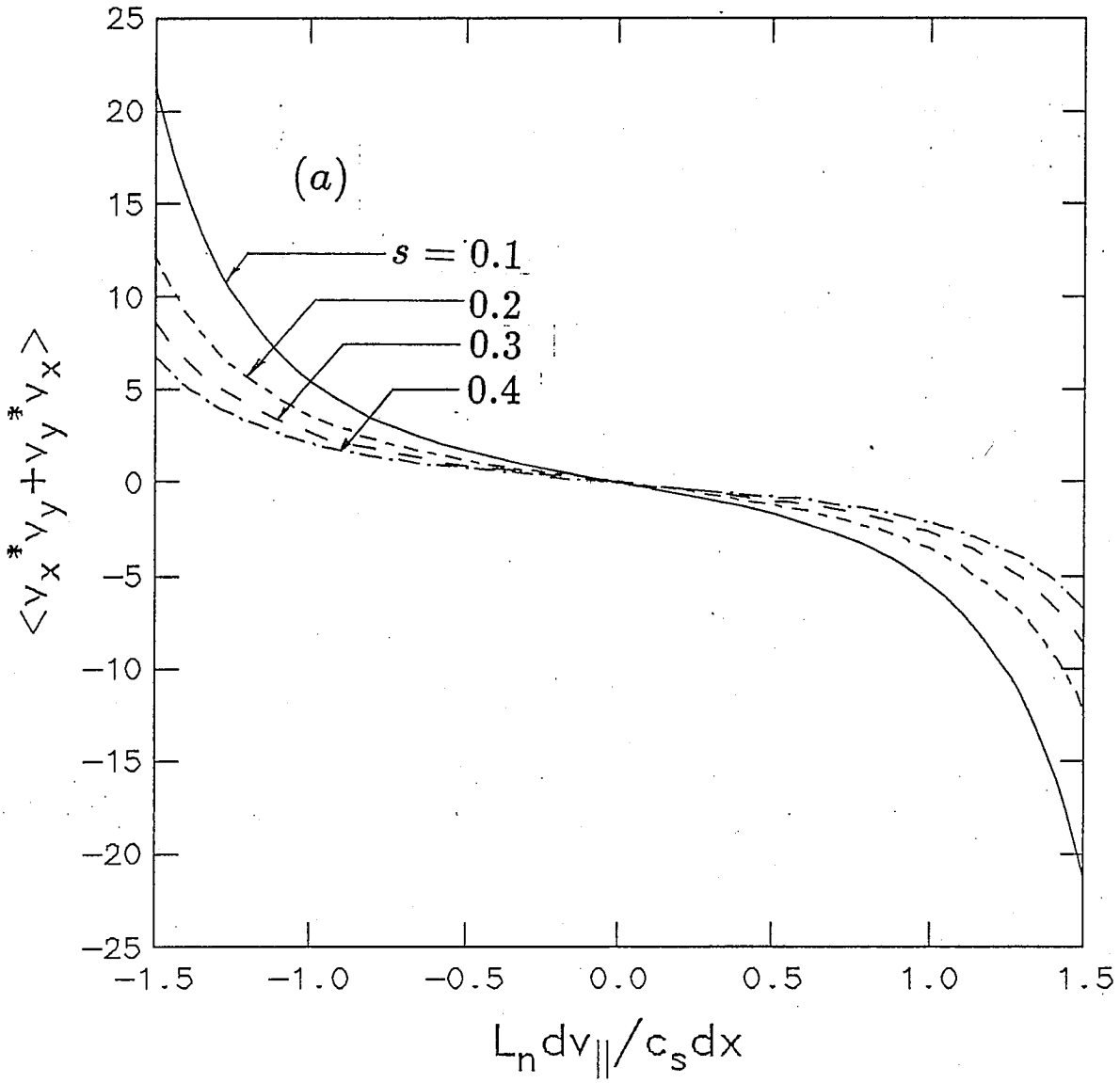
25
20
15
10
5
0
−5
−10
−15
−20
−25
−1.5
−1.0
−0.5
0.0
0.5
1.0
1.5
(a)
s = 0.1
0.2
0.3
0.4
<v_x* v_y + v_y* v_x>
L_n dv_|| / c_s dx

Fig. 3

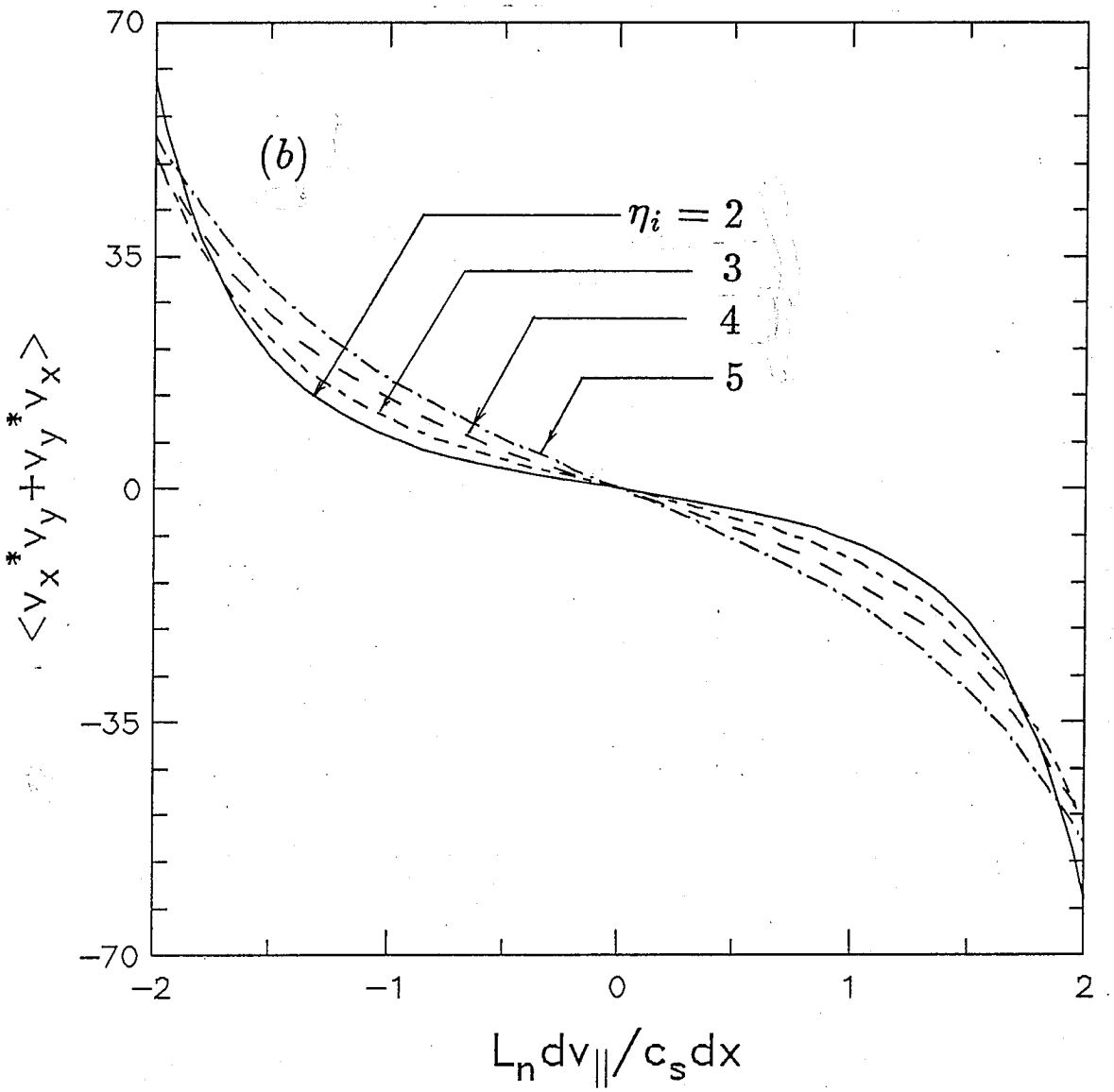
70
35
0
−35
−70
−2
−1
0
1
2
(b)
$\eta_i = 2$
3
4
5
$\langle v_x^* v_y + v_y^* v_x \rangle$
$L_n dv_{||}/c_s dx$

Fig. 3

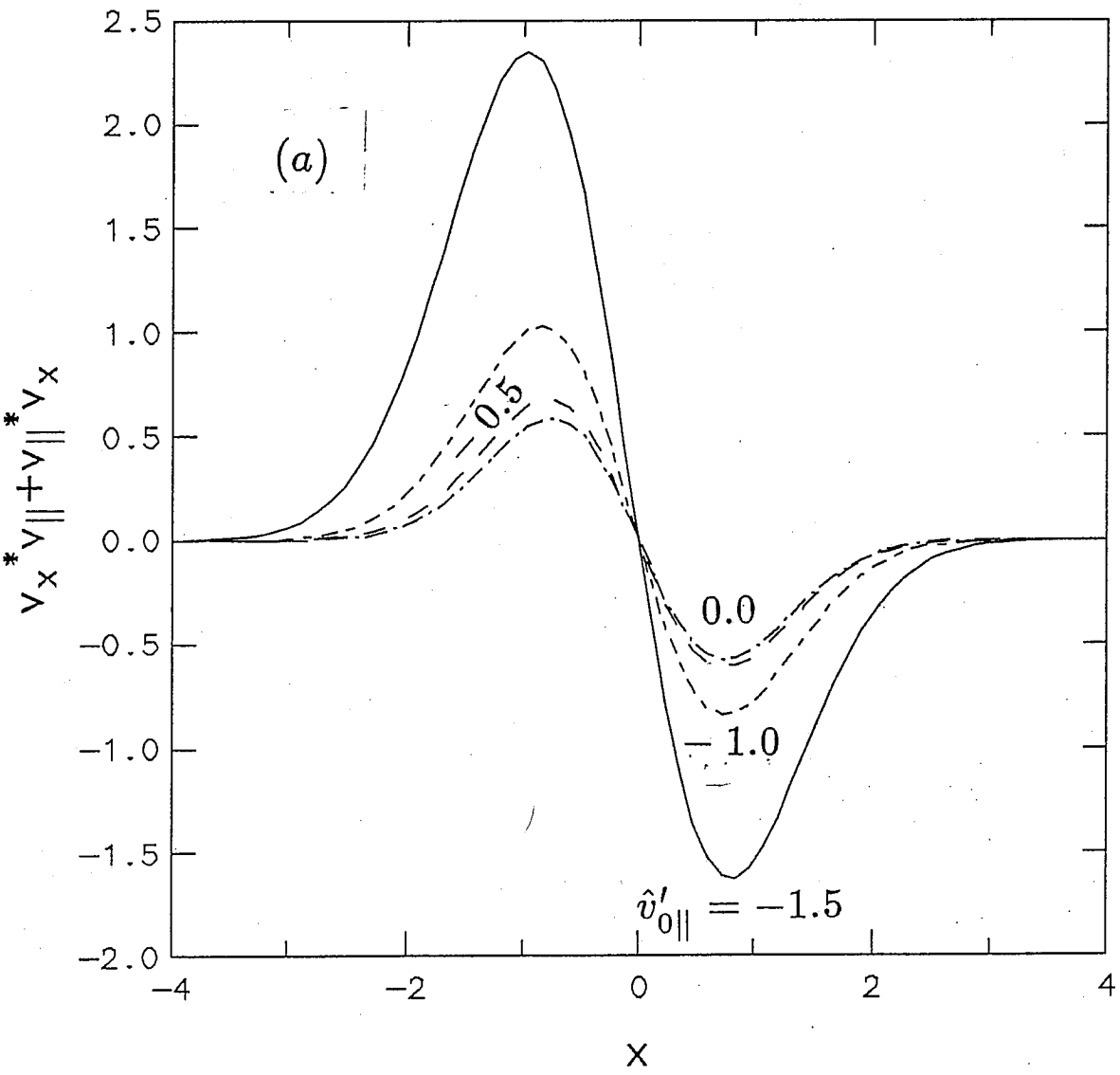

Fig. 4

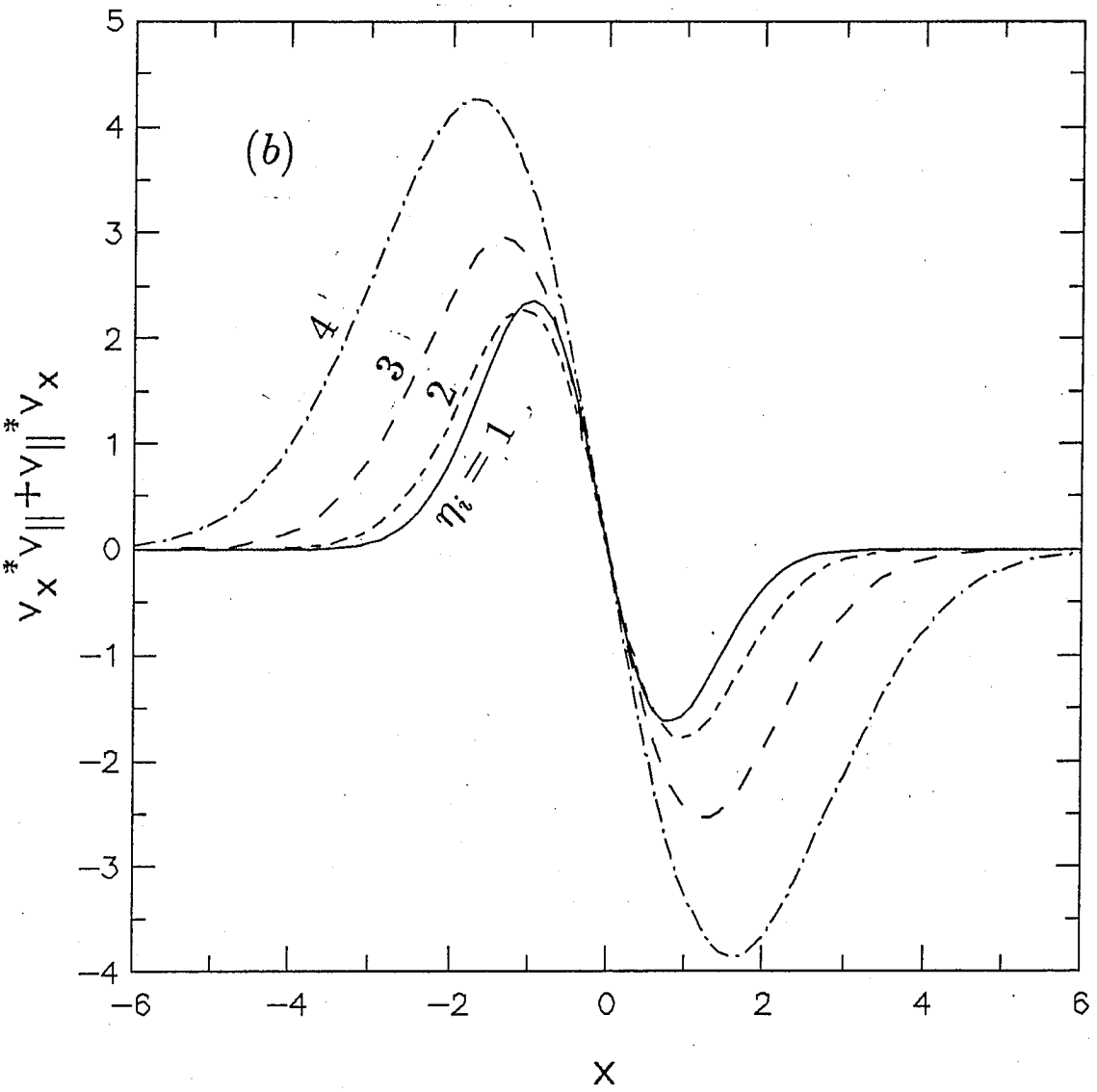

Fig. 4

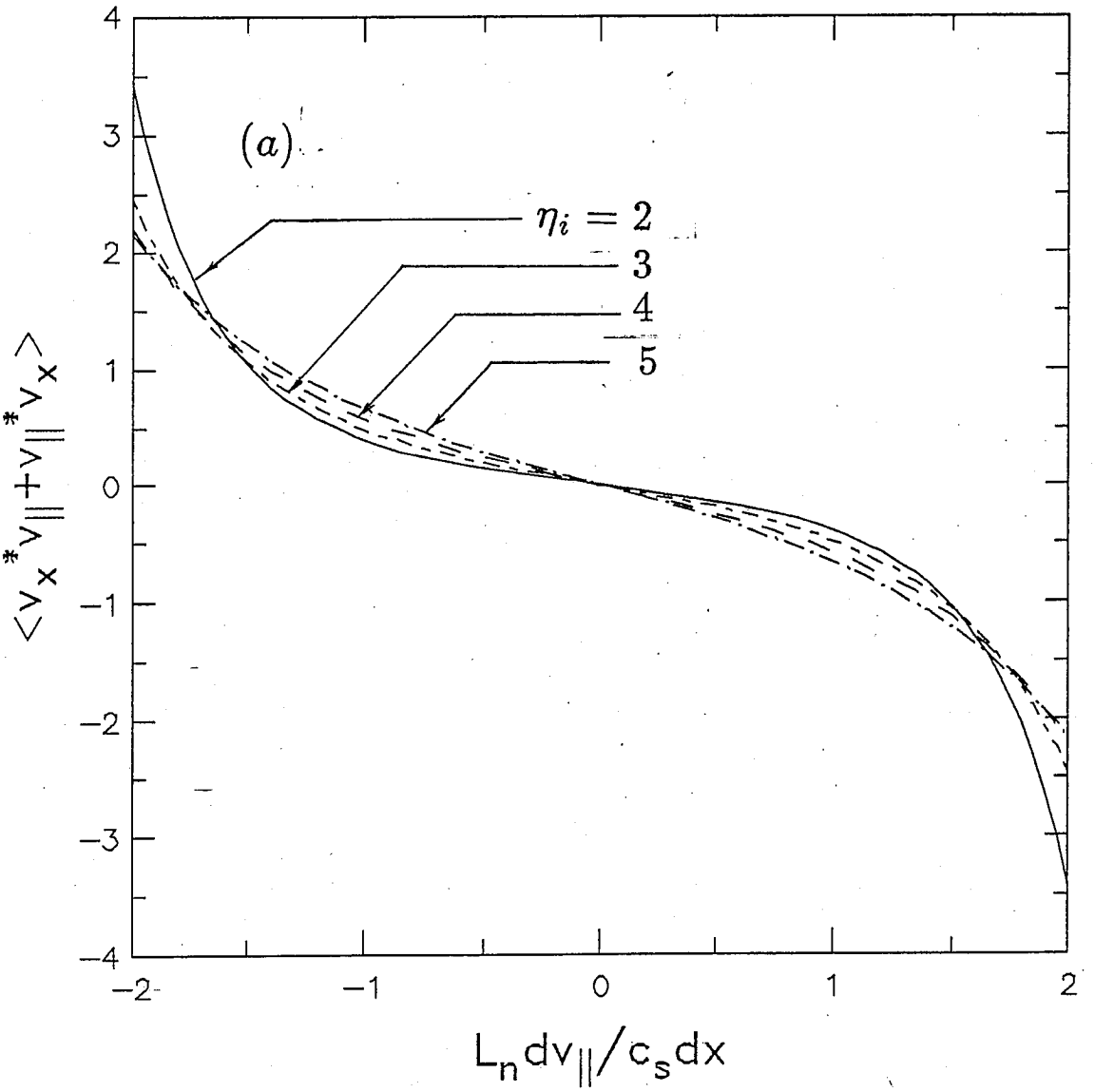

Fig. 5

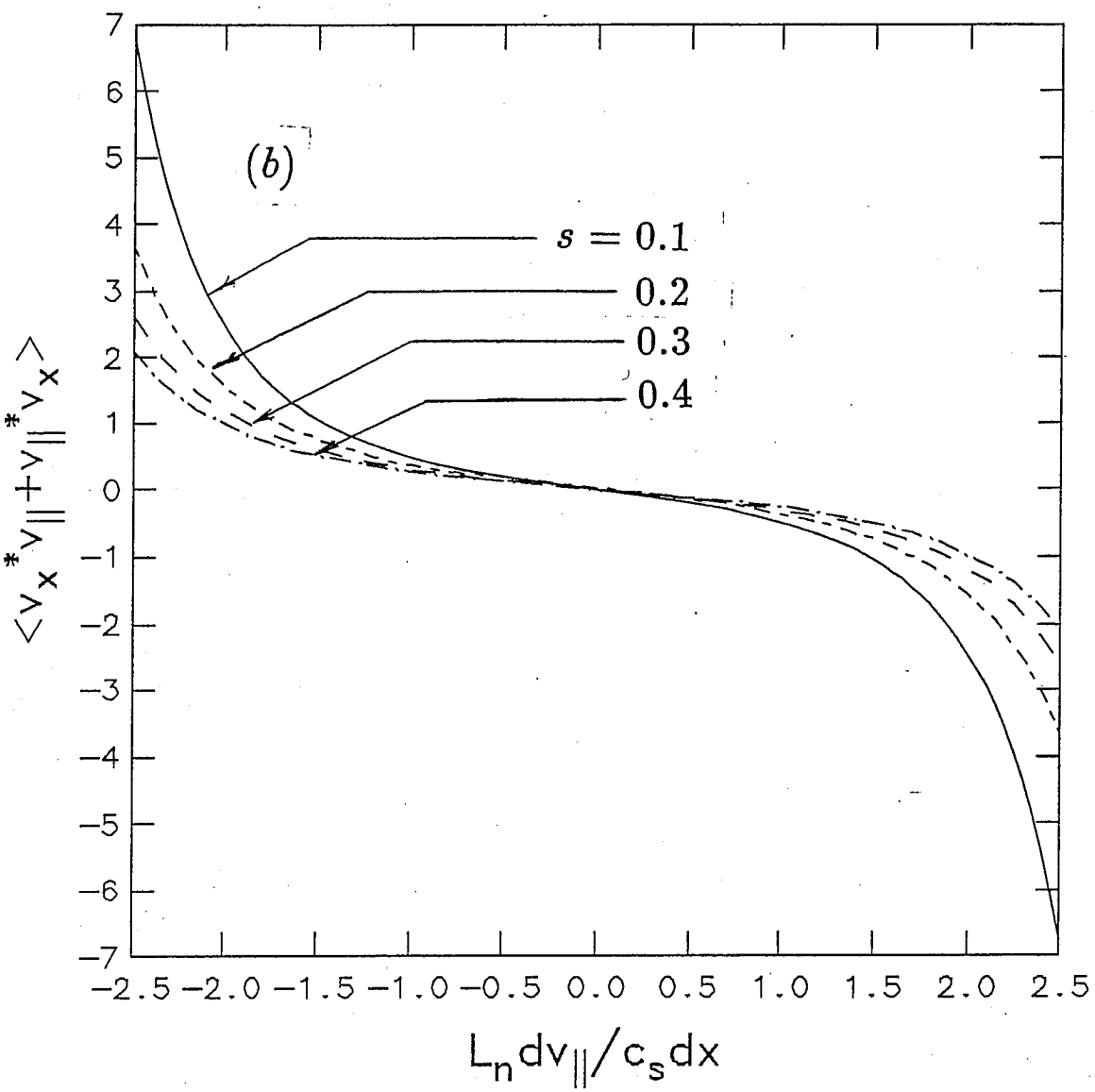
(b)
s = 0.1
0.2
0.3
0.4
$\langle v_x^* v_{||} + v_{||}^* v_x \rangle$
$L_n dv_{||}/c_s dx$
7
6
5
4
3
2
1
0
−1
−2
−3
−4
−5
−6
−7
−2.5 −2.0 −1.5 −1.0 −0.5 0.0 0.5 1.0 1.5 2.0 2.5

Fig. 5

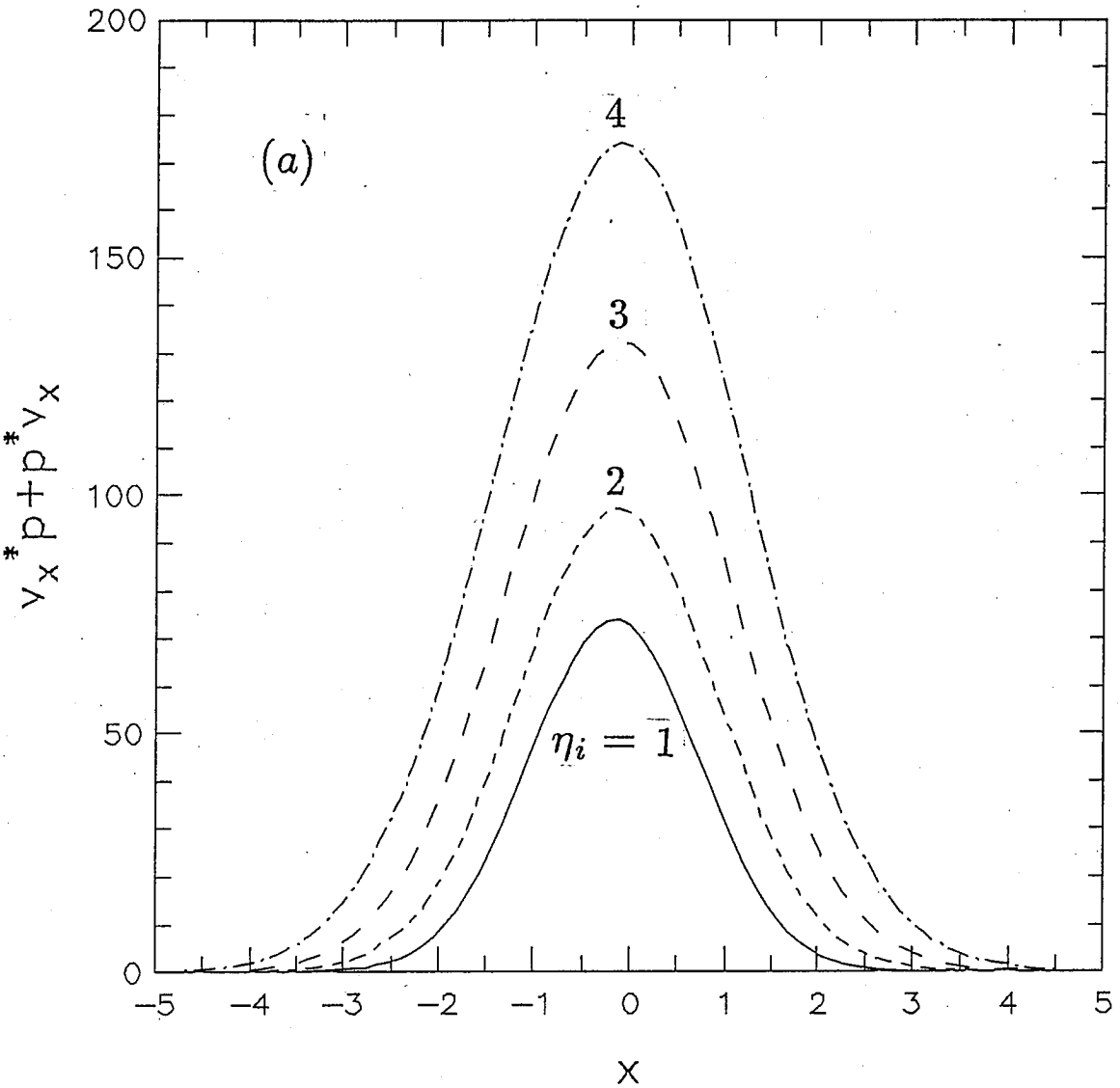

Fig. 6

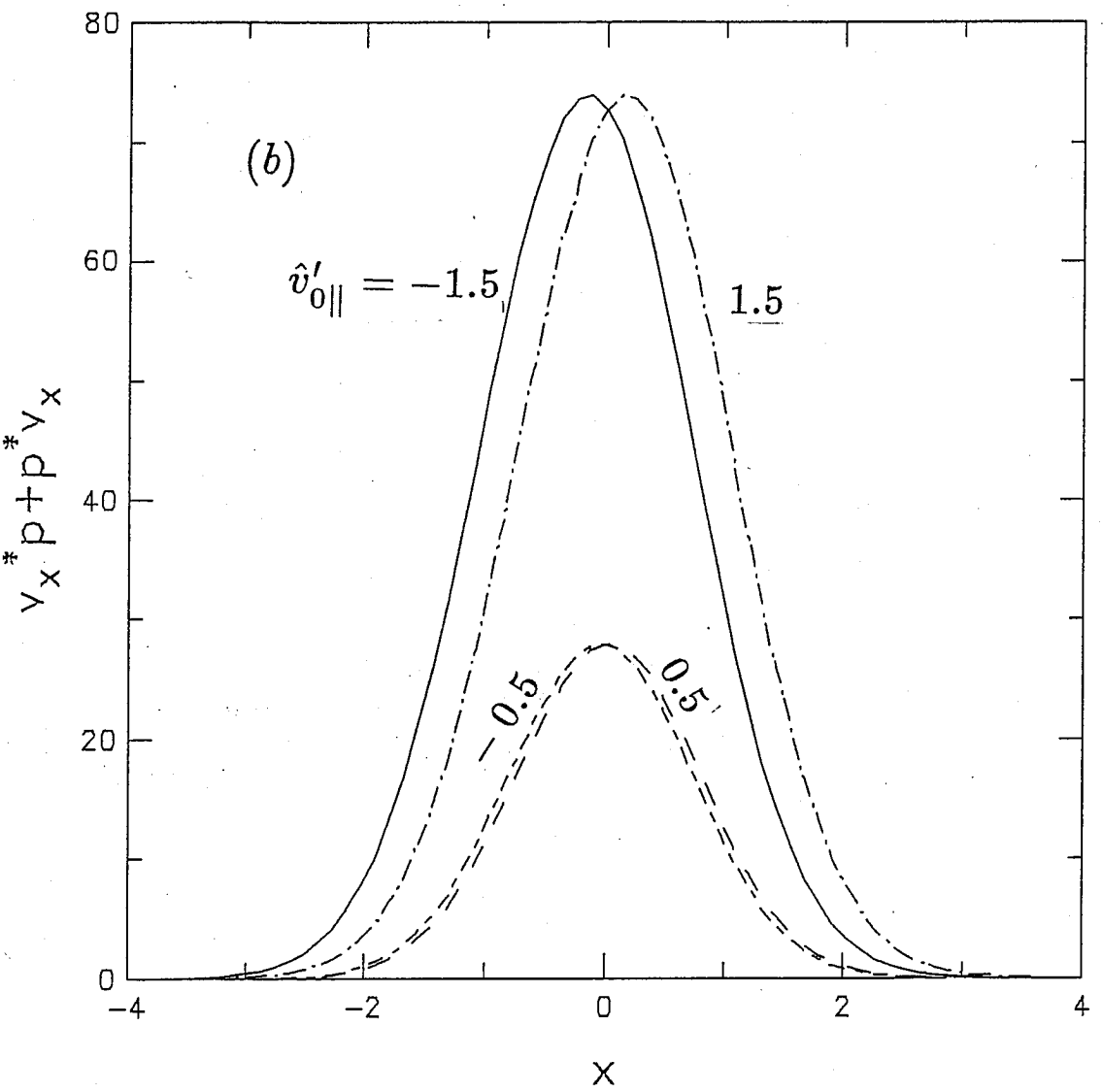

Fig. 6

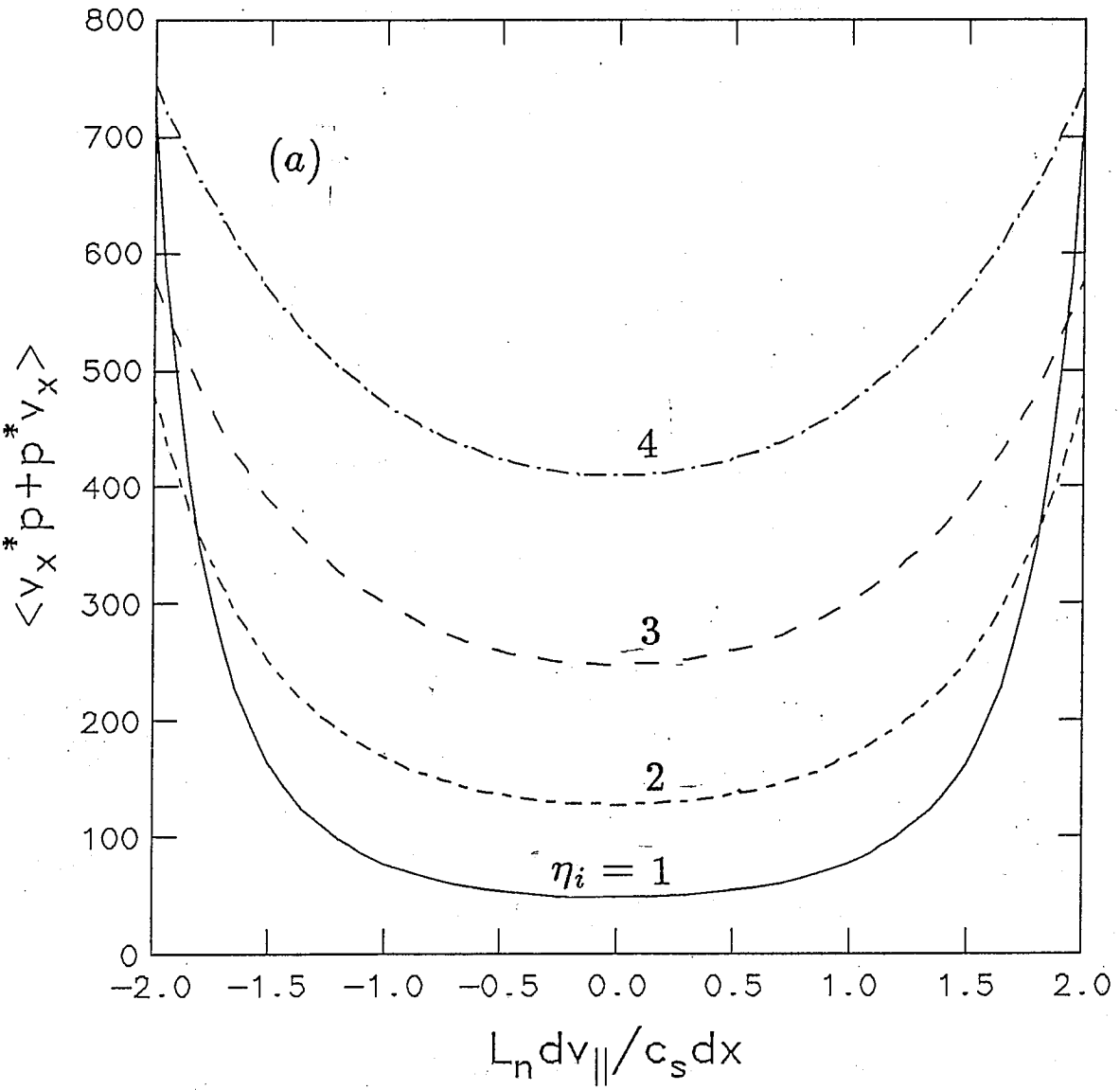

Fig. 7

Dong, PoP 20505

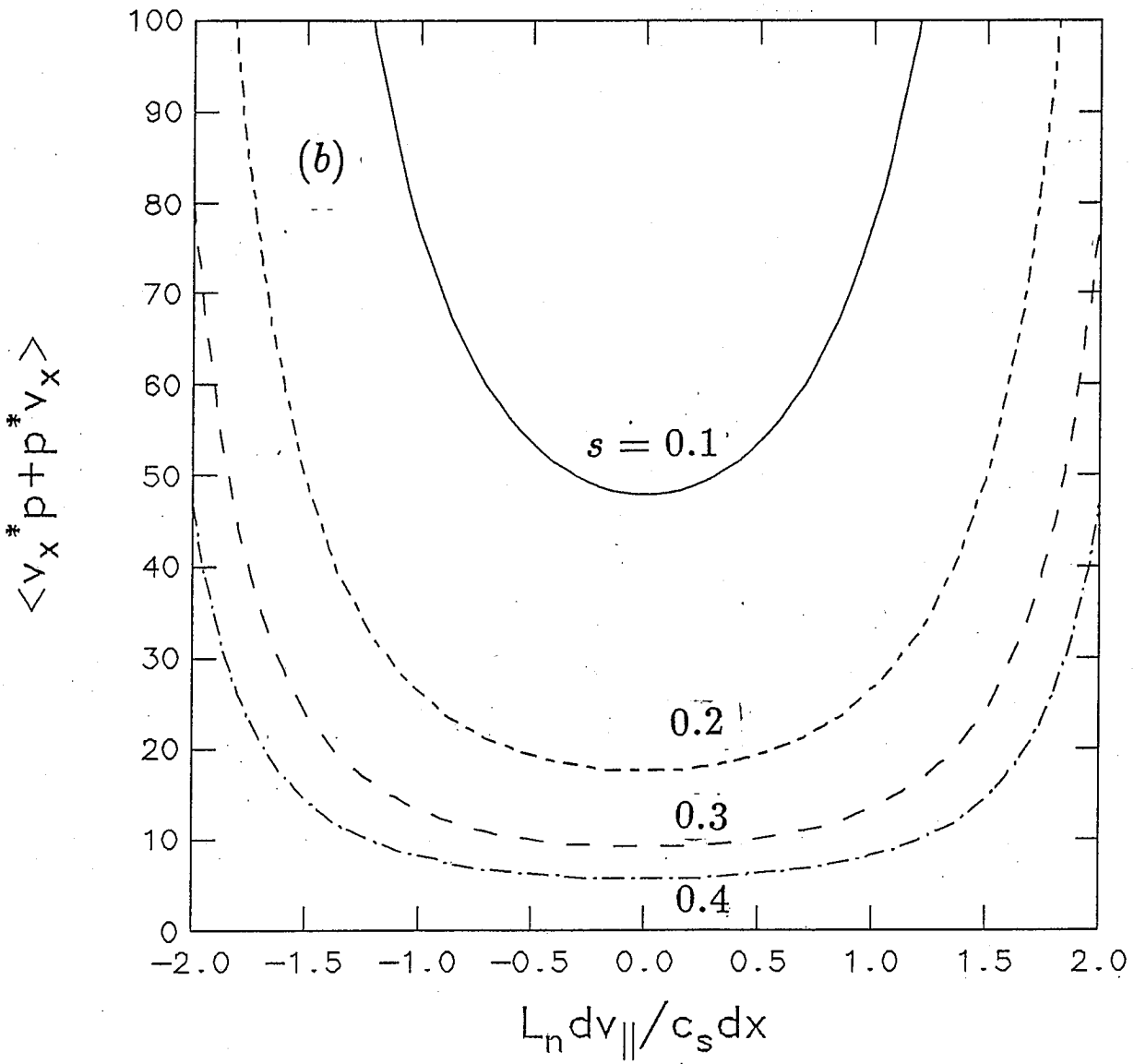

Fig. 7

Dong, PoP 20505

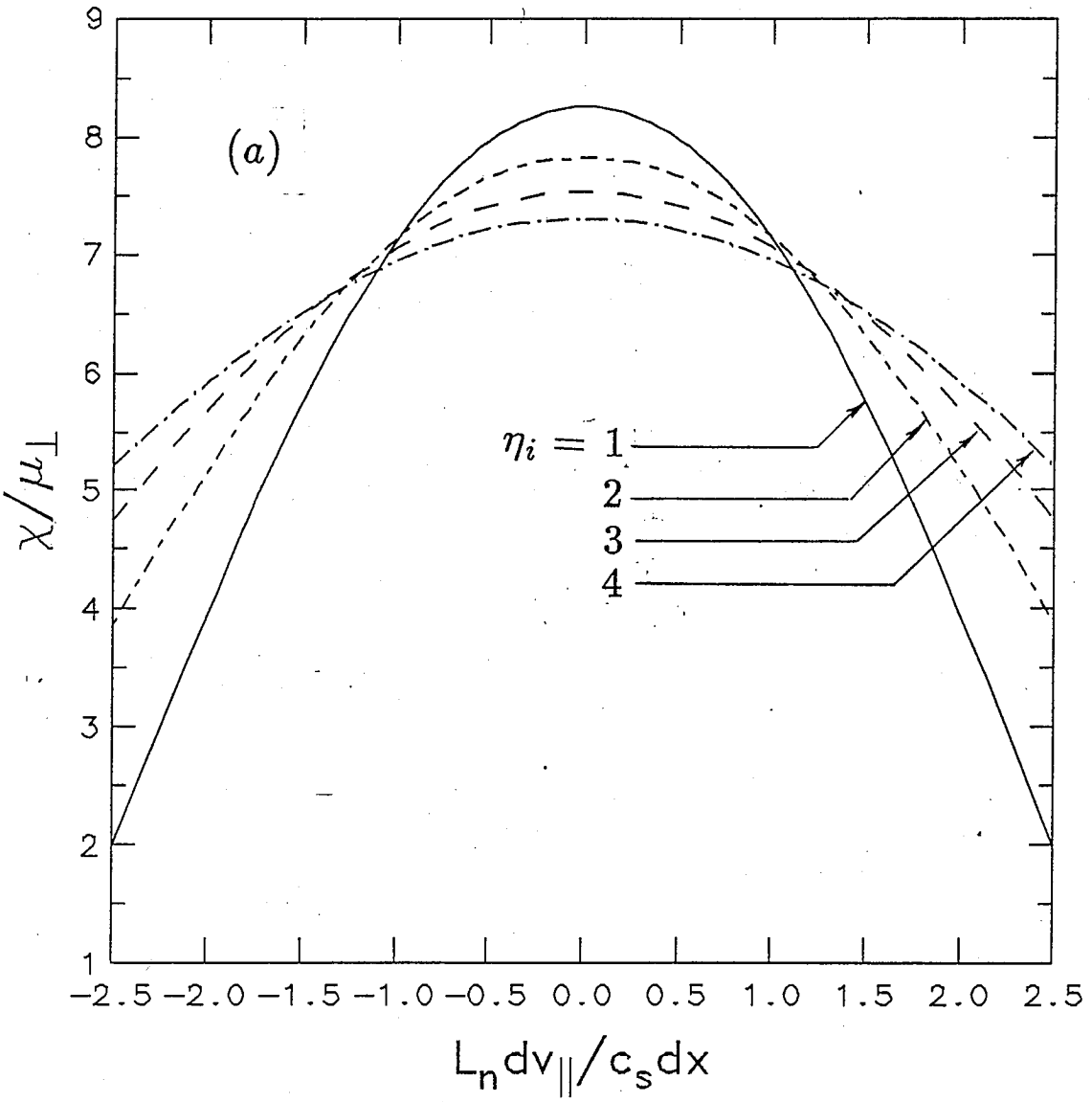

Fig. 8

Dong, PoP 20505

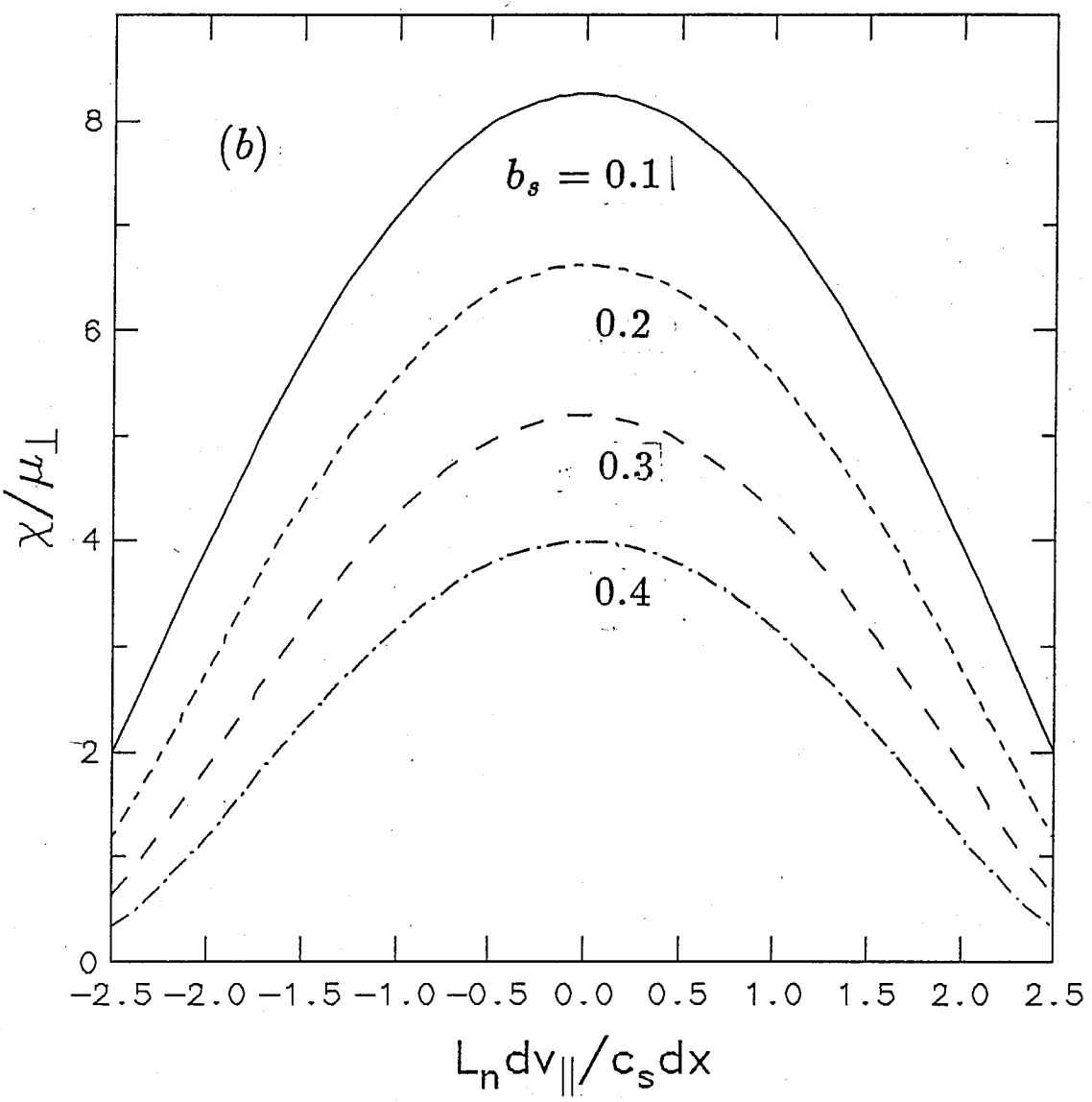

Fig. 8

Dong, PoP 20505

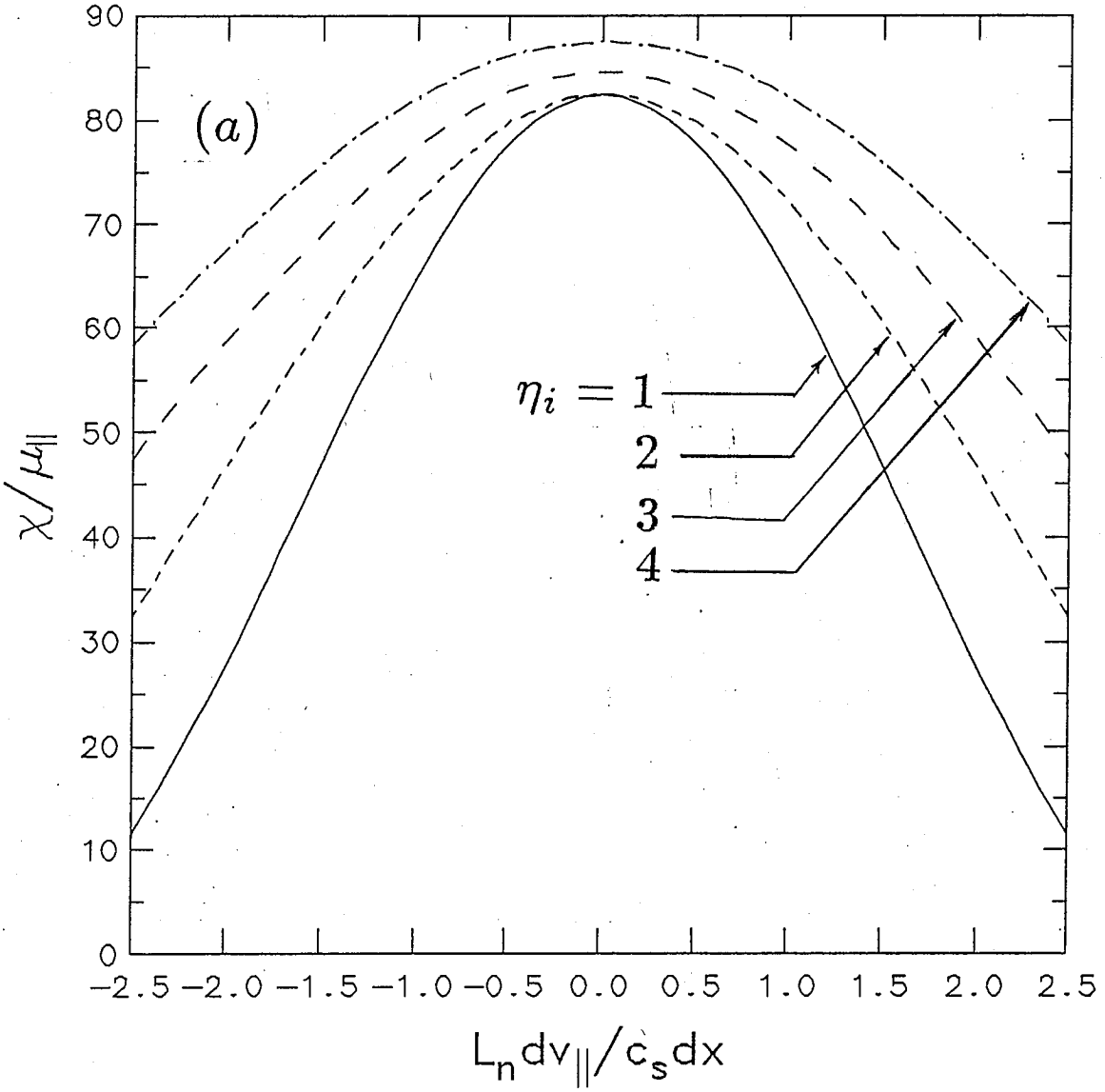
(a)
$\eta_i = 1$
2
3
4
$\chi/\mu_{\|}$
$L_n dv_{\|}/c_s dx$
90
80
70
60
50
40
30
20
10
0
−2.5 −2.0 −1.5 −1.0 −0.5 0.0 0.5 1.0 1.5 2.0 2.5

Fig. 9

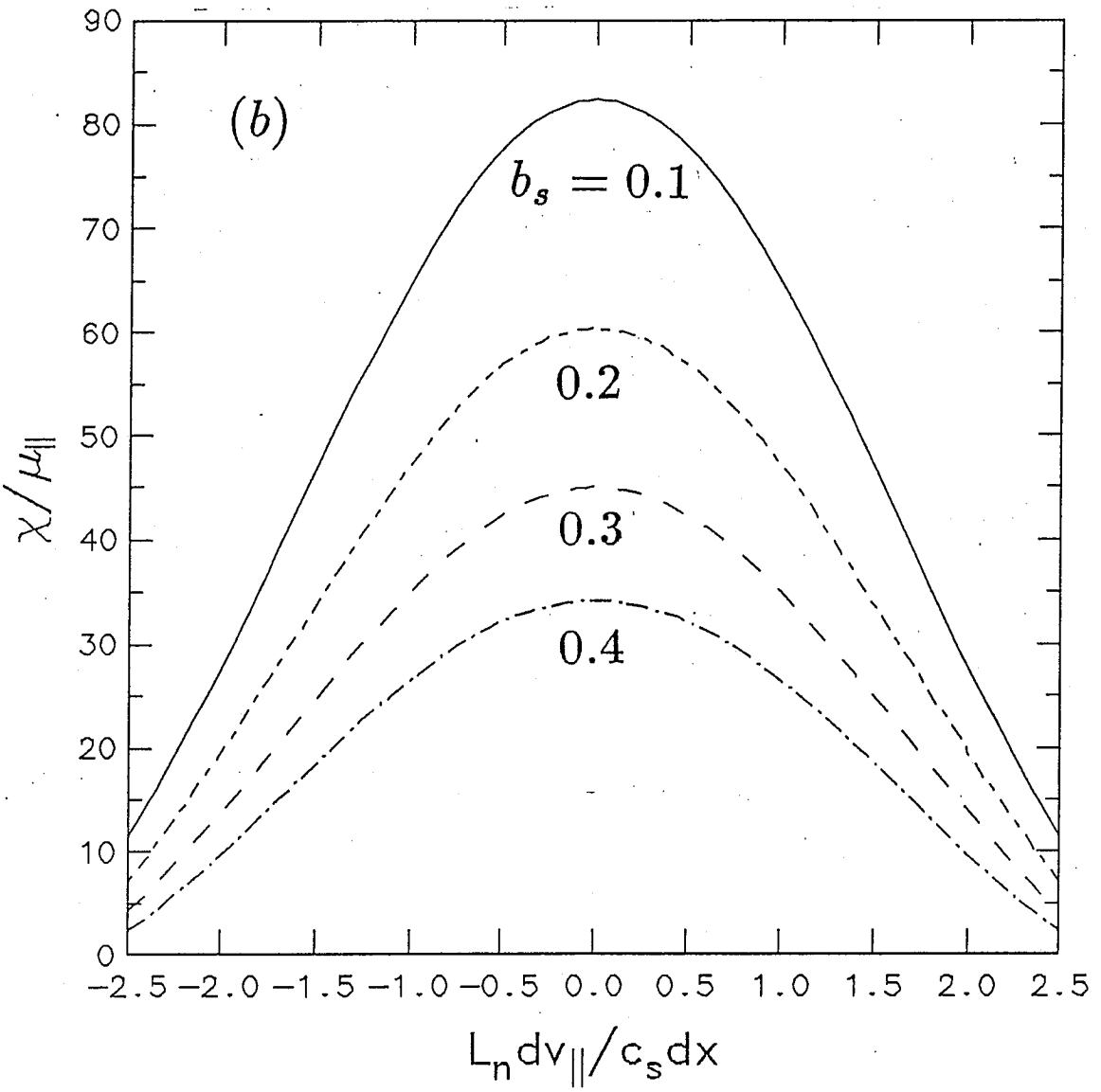

Fig. 9

Dong, PoP 20505

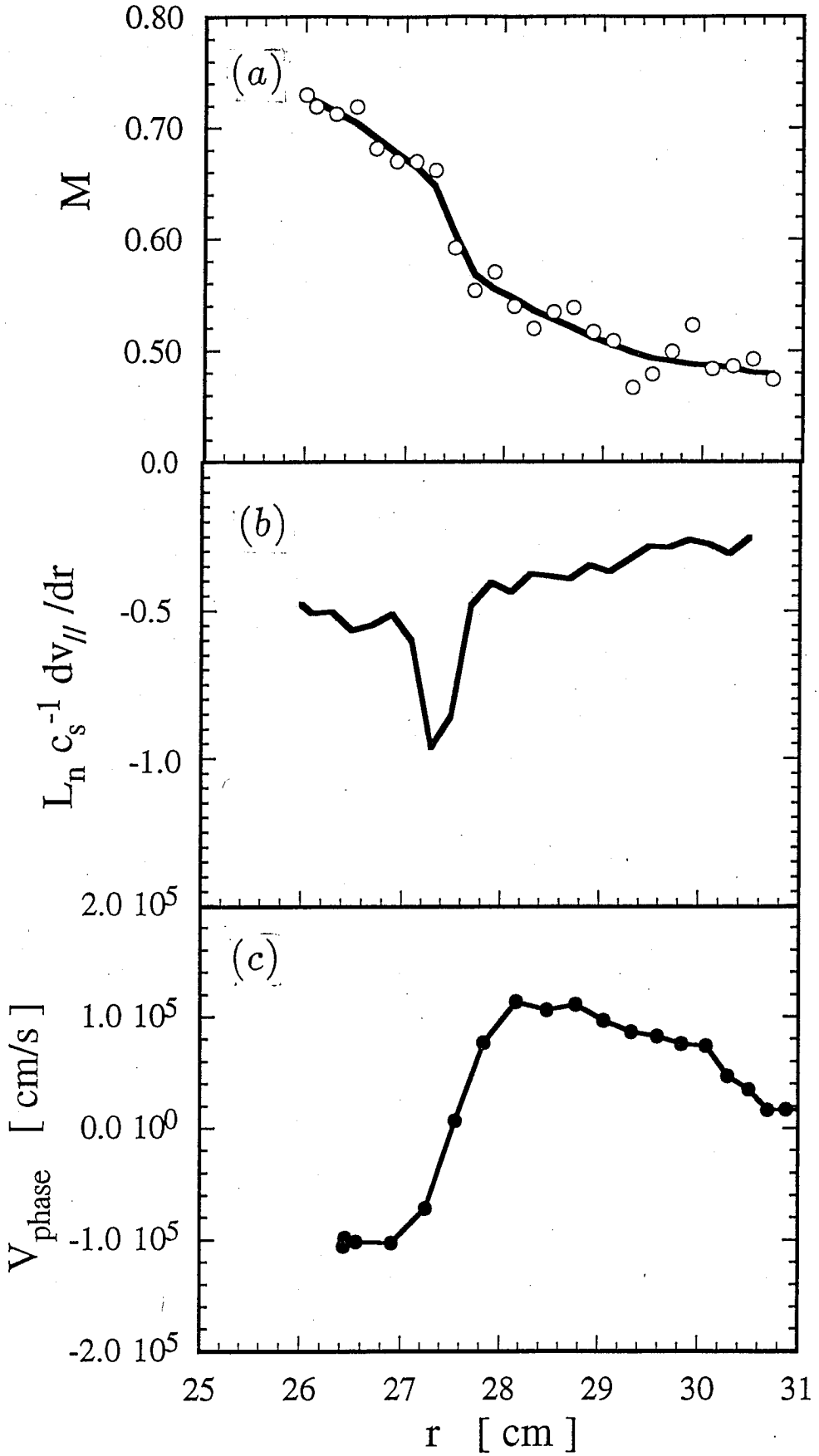

Fig. 10

Dong, PoP 20505

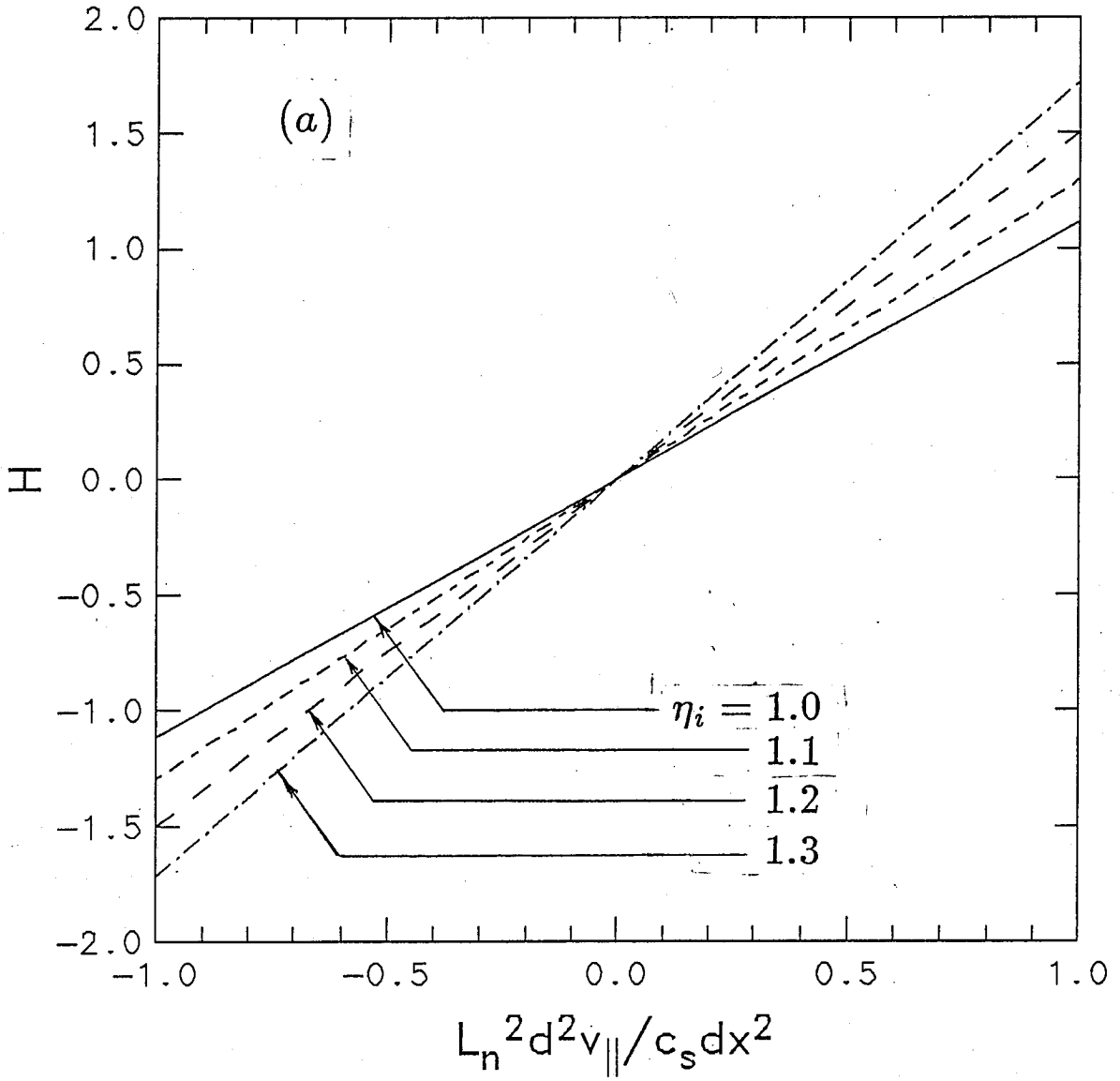

Fig. 11

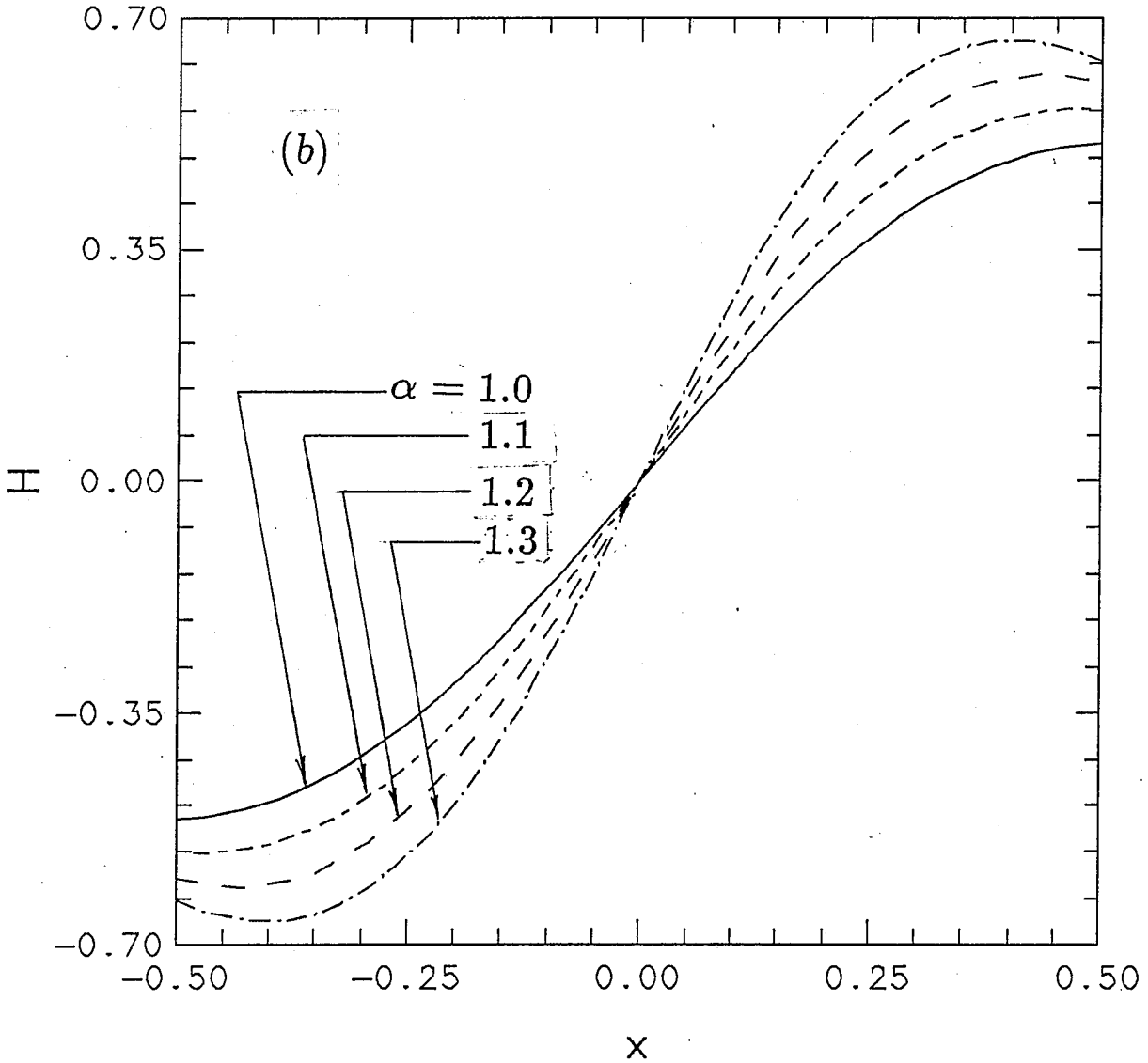

Fig. 11